



## Structure and Properties of Madden–Julian Oscillations Deduced from DYNAMO Sounding Arrays

RICHARD H. JOHNSON AND PAUL E. CIESIELSKI

*Colorado State University, Fort Collins, Colorado*

(Manuscript received 21 February 2013, in final form 8 May 2013)

### ABSTRACT

The kinematic and thermodynamic characteristics of the October and November 2011 Madden–Julian oscillations (MJOs) that occurred over the Indian Ocean during Dynamics of the MJO (DYNAMO) are investigated. Analyses are presented 1) for two primary sounding arrays, where results are independent of model parameterizations, and 2) on larger scales, including the Indian Ocean, using operational and reanalysis data.

Mean precipitation during DYNAMO was characterized by maxima in two east–west bands north and south of the equator. This pattern alternated between two bands during the inactive phase of the MJOs and a single rainfall maximum on the equator during the active phases. Precipitation over the northern sounding array (NSA), where the MJO signal was strongest, was significantly modulated by the MJOs, while the southern array experienced more frequent, briefer episodes of rainfall mostly related to ITCZ convection. Over the NSA the MJOs were characterized by gradual moistening of the low to midtroposphere over approximately 2-week periods. The October MJO featured multiple westward-moving, 2-day disturbances whereas the November MJO principally comprised two prominent Kelvin waves. Patterns of moistening, divergence, and vertical motion suggest a stepwise progression of convection, from shallow cumulus to congestus to deep convection. Tilted thermal anomalies in the upper troposphere–lower stratosphere reveal gravity or Kelvin waves excited by the MJO convective envelopes, which modulate the tropopause and contribute to preactive-phase upper-tropospheric moistening. While there is a number of similarities in the characteristics of the two MJOs, there are sufficient differences to warrant caution in generalizing results from these two events.

### 1. Introduction

The Madden–Julian oscillation (MJO; Madden and Julian 1972) is the most dominant signal of intraseasonal variability in the tropics. Its impacts are far reaching. They extend into the subtropics and midlatitudes; specifically, there are influences on tropical cyclone frequency, monsoon onset and rainfall variability, ENSO, mid-latitude storm tracks, the North Atlantic Oscillation, the Arctic and Antarctic Oscillations, the Indian Ocean dipole, Wyrтки jets, Indonesian Throughflow, and seasonal heat transport in the Indian Ocean (Webster et al. 1999; Lau and Waliser 2005; Wang 2005; Zhang 2005; Waliser 2006). Despite considerable attention given to the MJO over the past several decades, deficiencies remain in its

basic understanding and prediction. Coupled general circulation models have a difficult time accurately simulating the MJO (Lin et al. 2006; Hung et al. 2013) and there is limited skill in prediction models (Kim et al. 2009). Moreover, recent work questions the nature of the MJO itself, suggesting that MJO disturbances are not dynamically distinct modes from equatorial Kelvin waves (Roundy 2012a,b). Hence, the basic dynamics of the MJO still remain an enigma.

Significant progress was achieved in observing basic features of the MJO in the western Pacific based on data from the 1992/93 Tropical Ocean and Global Atmosphere Coupled Ocean–Atmosphere Response Experiment (TOGA COARE), particularly the ocean–atmosphere coupling, the evolving precipitation systems, westerly wind bursts, surface fluxes, and the behavior of equatorial waves (Godfrey et al. 1998). However, conditions over the western Pacific are different from those over the Indian Ocean where deep convection associated with the MJO most frequently originates. The Indian Ocean is

---

*Corresponding author address:* Richard H. Johnson, Department of Atmospheric Science, 1371 Campus Delivery, Colorado State University, Fort Collins, CO 80523.  
E-mail: johnson@atmos.colostate.edu

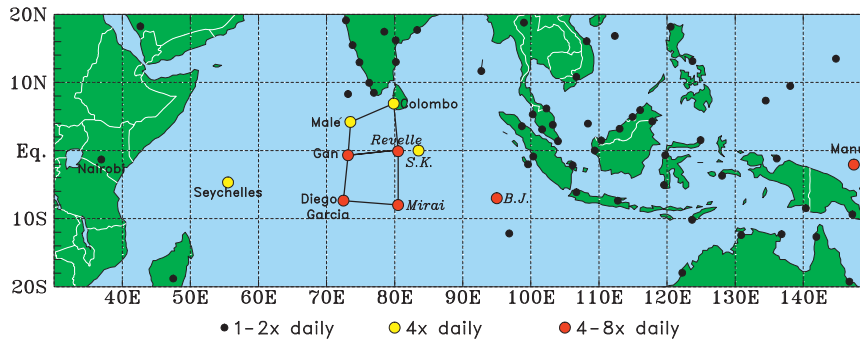


FIG. 1. DYNAMO/CINDY/AMIE sounding network for the period October–December 2011. Analysis domain includes high-frequency soundings (4 and 8  $\text{day}^{-1}$ ; yellow and red dots, respectively) and priority sounding sites (1 or 2  $\text{day}^{-1}$ ; black dots). Data from R/V *Sagar Kanya* (S. K.) and R/V *Baruna Jaya* (B. J.), which were on station for brief periods (25 Sep–19 Oct for S. K. and 5–18 Dec for B. J.), were also utilized in the analyses.

surrounded by landmasses on three sides and features seasonally reversing mean flow associated with the strongest monsoon in the world. The thermocline in the western Pacific is relatively deep, such that entrainment cooling only occasionally contributes to the upper-ocean heat budget (Lukas and Lindstrom 1991; Cronin and McPhaden 1997), whereas the Indian Ocean features the relatively shallow Seychelles–Chagos thermocline ridge that exhibits large intraseasonal SST variability (Hermes and Reason 2008; Vialard et al. 2009). Furthermore, unlike the Indian Ocean, the western Pacific can exhibit a unique coupling between the MJO and the ocean by exciting oceanic Kelvin waves that then interact with convection (Roundy and Gribble-Verhagen 2010).

Given the pronounced intraseasonal variability of the SST in the Indian Ocean, there is strong evidence that ocean–atmosphere coupling plays an important role in MJO dynamics in that basin (Flatau et al. 1997; Stephens et al. 2004; Zhang 2005). A sequence of events in MJO development has been hypothesized to proceed as follows. During the initiation phase, shallow cumuli progressively deepen into congestus clouds, the lower troposphere moistens, and the upper ocean warms. These processes result in a buildup of convective instability. This period has come to be referred to as the “recharge phase” of the MJO (Bladé and Hartmann 1993; Hu and Randall 1994; Kemball-Cook and Weare 2001), during which moistening of the lower troposphere is achieved via detrainment from cumulus and congestus clouds (Johnson et al. 1999; Kikuchi and Takayabu 2004) and/or moisture advection (Benedict and Randall 2009; Maloney 2009). During the active phase of the MJO, deep convection ensues, the upper troposphere moistens, and the upper ocean cools as a result of increased convective activity leading to reduced shortwave radiation, enhanced surface fluxes, and upper-ocean mixing (Shinoda and Hendon

1998). Following the most intense rainfall, the precipitation systems become more stratiform in character, strong low-level winds develop, the upper ocean cools further, and the mid- to lower troposphere rapidly dries out (Lin and Johnson 1996; Maloney and Hartmann 1998; Johnson et al. 1999; Benedict and Randall 2009).

The evolution of precipitation systems and diabatic heating throughout this process can be broadly characterized as a transition from shallow cumulus to cumulus congestus to deep convection to stratiform (Johnson et al. 1999; Kikuchi and Takayabu 2004; Kiladis et al. 2005; Benedict and Randall 2007; Haertel et al. 2008). Recent measurements from *CloudSat* and *Cloud–Aerosol Lidar and Infrared Pathfinder Satellite Observations* (CALIPSO) have provided additional documentation of the cloud fields associated with the MJO (Virts and Wallace 2010; Riley et al. 2011; Del Genio et al. 2012). These studies suggest that rather than cloud populations smoothly evolving from one type to another throughout the MJO life cycle, all cloud types occur to some extent in all MJO phases but their frequency of occurrence varies with time so as to give the broad appearance of a smooth transition. These findings support the “building block” concept of the MJO proposed by Mapes et al. (2006). But more specifically, there is evidence from the studies of Kikuchi and Takayabu (2004), Yoneyama et al. (2008), Virts and Wallace (2010), and Del Genio et al. (2012) to indicate that this progression of the cloud population actually occurs in a stepwise fashion, with distinct periods of about 1 week or more when there is a dominance of each (cumulus, congestus, cumulonimbus) cloud type.

Despite these advances, the mechanisms by which the atmosphere is moistened during the initiation phase of the MJO are still not fully understood. In fact, this subject remains a matter of considerable debate (Waite and

TABLE 1. Sounding sites comprising quadrilateral arrays for the SOP (1 Oct–15 Dec 2011). Ship locations are nominal positions; they neglect minor on-station maneuvering and port calls.

Station	Location	Elevation (m)	Instrument type	No. of SOP soundings
Gan Island	0.69°S, 73.15°E	1	Vaisala RS92	620
R/V <i>Revelle</i>	0.00°N, 80.50°E	19	Vaisala RS92	444
Diego Garcia	7.31°S, 72.43°E	2	Vaisala RS92	513
R/V <i>Mirai</i>	8.00°S, 80.50°E	18	Vaisala RS92	485
Malé	4.19°N, 73.53°E	2	Vaisala RS92	320
Colombo	6.91°N, 79.87°E	15	Meisei RS06G	255

Khouider 2010; Hohenegger and Stevens 2013). To address this problem, a field campaign was recently conducted in the Indian Ocean during the period October 2011–March 2012. Its overarching goal was to investigate mechanisms contributing to the initiation of the MJO. The experiment comprised three principal participating entities: Dynamics of the MJO (DYNAMO), Cooperative Indian Ocean Experiment on Intraseasonal Variability in the Year 2011 (CINDY2011), and the Atmospheric Radiation Measurement Program (ARM) MJO Investigation Experiment (AMIE) (Yoneyama et al. 2013; Zhang et al. 2013). The collective field campaign effort will be referred to as DYNAMO. DYNAMO's three main objectives are 1) determination of the mechanisms by which the troposphere is moistened in the initiation stage of the MJO, 2) the role of cloud populations in MJO initiation, and 3) the role of air–sea interaction in the development and evolution of the MJO. While studies have been conducted concerning these processes, they have principally been based upon reanalysis products and satellite data. The only prior field efforts in the Indian Ocean directed at these objectives have been the 2006 *Mirai* Indian Ocean Cruise for the Study of the MJO Onset (MISMO; Yoneyama et al. 2008) experiment and the French Vasco–Cirene experiment (Vialard et al. 2009), but these field campaigns have been limited in scope compared to DYNAMO.

This paper reports on preliminary findings from DYNAMO related to the broad-scale structure and properties of the two prominent MJOs that occurred during the October–November 2011 period of DYNAMO [the special observing period (SOP)] as revealed by the atmospheric sounding arrays. A unique aspect of DYNAMO that contrasts it with TOGA COARE is its location in the Indian Ocean where coupling of the MJO with deep convection first occurs (Madden and Julian 1972). While our eventual goal is to unravel the mechanisms operative during the moistening phase of the MJOs, the achievement of this objective will involve a comprehensive analysis of large-scale moisture budgets, cloud populations, air–sea interaction, etc. Such an effort will require the integration of multiple datasets including ground-based radars, lidars, soundings, aircraft, and satellites—a task

underway but not yet completed. Therefore, the objective of this paper is to document the basic thermodynamic and kinematic structure of the large-scale environment to provide a context for that future work. The unique measurements collected during DYNAMO provide an unprecedented dataset over the Indian Ocean with which to establish this large-scale environmental setting.

## 2. Data and analysis procedures

### a. Sounding observations

The DYNAMO sounding network comprised two quadrilateral arrays: one north and one south of the equator (Fig. 1). The designs of the arrays were largely dictated by the locations of suitable facilities on islands and atolls. Prior to the experiment, a study was conducted to evaluate the accuracy of quadrilateral arrays from the standpoint of budget computations. It was demonstrated that such arrays represented an improvement over the triangular array used during MISMO in capturing wave components of the MJO (Katsumata et al. 2011).

The six sounding sites comprising the two quadrilateral arrays shown in Fig. 1 are listed in Table 1. These arrays were intact for the majority of the 1 October–15 December time frame, so this period is selected as the focus of our study.<sup>1</sup> The southern quadrilateral reverted to a triangular array from 25 to 30 October during the research vessel (R/V) *Mirai* port call after 30 November when the *Mirai* left its southern post and from 31 October to 7 November during the R/V *Revelle* port call. Also, during this latter period, the northern array collapsed to a triangle. Finally, from 8 to 16 December, the *Revelle* was once again off station, so a southern array did not exist then. During these periods, computed fields of divergence and vertical motion are less reliable (Katsumata et al. 2011), so the port-call intervals will be highlighted in subsequent figures. The four sites in the southern array launched eight soundings per day, while Malé and Colombo had a launch schedule of four soundings per day,

<sup>1</sup> While this period is 15 days longer than the official DYNAMO SOP, to simplify terminology it will be referred to as the SOP.

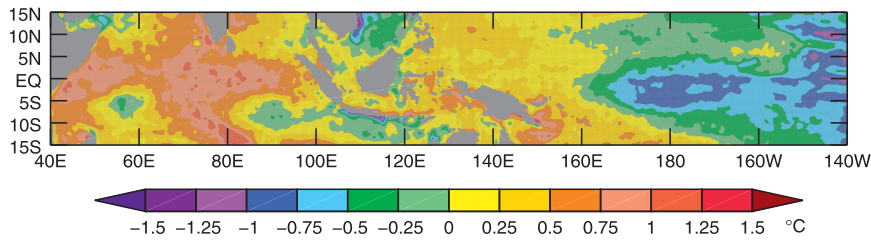


FIG. 2. Sea surface temperature anomalies ( $^{\circ}\text{C}$ ) from the long-term (1981–2012) mean over the tropical Pacific and Indian Oceans during the DYNAMO period 1 Oct–15 Dec 2011, based on Reynolds et al. (2007) high-resolution blended analysis.

with Colombo falling back to one sounding per day after 5 December. Five sites used Vaisala RS92 sounding systems (Table 1), while Colombo operated a Meisei RS06G system. All sites employed GPS wind-finding capabilities.

As of this writing, sounding data quality control procedures, which mainly involve humidity corrections, are still under way. Preliminary intercomparisons with independent total column water measurements indicate that the RS92 systems exhibit a slight dry bias during the daytime. This dry bias is considerably less than that associated with earlier Vaisala sonde types (Wang and Zhang 2008). In particular, first indications are that the dry bias of the RS92 sensors (approximately 1%–2% in the lower troposphere and 5%–6% in the upper troposphere) is roughly only a third of that of the RS80 sensors used in TOGA COARE (Wang et al. 2002; Ciesielski et al. 2003). The Meisei system also has a biases that vary with altitude (Ciesielski et al. 2010), although corrections at Colombo have yet to be completed. Several Vaisala sites (Malé, Gan Island, *Mirai*) had built-in software to correct for a daytime dry bias, while a daytime bias correction adopted from Wang et al. (2013) was applied to the sondes from Diego Garcia and the *Revelle*. These humidity-corrected data will be used in this study. Future work that will focus on the moisture budgets for the MJO events will utilize relative humidity-corrected data at all sites.

In addition to corrections for sounding-humidity biases, work is in progress to correct for other sounding errors and siting impacts on the data and analyses thereof (e.g., ship heating effects, influences of Sri Lanka island flow blocking on low-level Colombo winds); however, these corrections or modifications to the soundings are largely excluded from this paper. Nevertheless, these effects, while potentially important for detailed investigations of the boundary layer properties and heat and moisture budgets, are not expected to alter the general conclusions of this study.

Finally, dropsonde data from the National Oceanic and Atmospheric Administration (NOAA) P-3 aircraft were incorporated into the gridded analyses described

below. There were 469 dropsonde observations from 13 flights in proximity to the sounding arrays during the period 9 November–13 December.

#### b. Other data sources

Precipitation rate estimates are based on the Tropical Rainfall Measuring Mission (TRMM) 3B42v7 product, which combines microwave rainfall estimates from TRMM and other satellites with high-temporal-resolution infrared rain-rate estimates to create a 3-hourly,  $0.25^{\circ} \times 0.25^{\circ}$  rainfall product (Huffman et al. 2007). Outgoing longwave radiation (OLR) data on a  $2.5^{\circ} \times 2.5^{\circ}$  grid are obtained from the NOAA/Earth System Research Laboratory (ESRL) (Liebmann and Smith 1996).

European Centre for Medium-Range Weather Forecasts (ECMWF) operational forecast data at  $0.25^{\circ}$  horizontal resolution, 18 vertical levels from the surface to 50 hPa, and 6-hourly intervals are used for the broad-scale analyses over the Indian Ocean, as well as north–south vertical cross sections extending beyond the sounding arrays. A majority ( $\sim 95\%$ ) of the data from the sounding arrays were transmitted to operational centers in real time, so the ECMWF analyses in the core sounding domain are heavily influenced by the sounding data and are in good agreement with our gridded analyses over the quadrilateral areas.<sup>2</sup> In addition, National Centers for Environmental Prediction (NCEP)–National Center for Atmospheric Research (NCAR) reanalyses (Kalnay et al. 1996) with  $2.5^{\circ}$  horizontal resolution, 15 vertical levels from the surface to 50 hPa, and 6-hourly intervals are used for vertical motion anomaly analyses.

Large-scale sea surface temperature (SST) observations were obtained from two sources. SST anomaly fields extending to the central Pacific are from the NOAA/ESRL website (<http://www.esrl.noaa.gov/psd/>)

<sup>2</sup> Comparison of sounding-array mean profiles of zonal and meridional winds and relative humidity between the ECMWF and our model-independent, interpolated analyses indicates agreement to within  $0.5 \text{ m s}^{-1}$  and 5%, respectively.

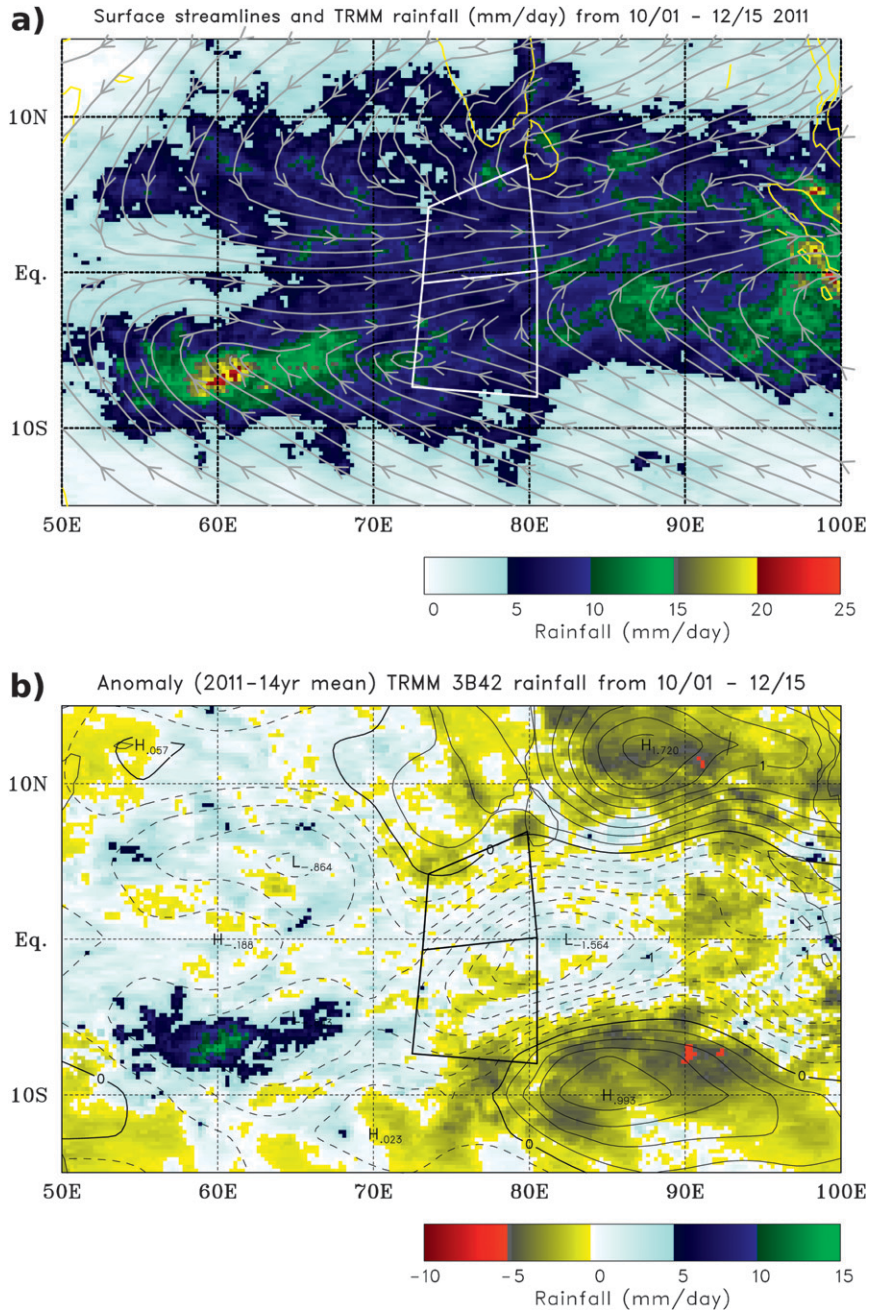


FIG. 3. (a) TRMM 3B42 precipitation ( $\text{mm day}^{-1}$ ) and ECMWF operational analysis surface streamlines and (b) TRMM 3B42 precipitation anomalies ( $\text{mm day}^{-1}$ ) and NCEP-NCAR reanalysis 500-hPa vertical  $p$ -velocity anomalies ( $\text{hPa h}^{-1}$ ) for the DYNAMO period 1 Oct–15 Dec 2011. Anomalies are computed from a 14-yr (1998–2011) mean corresponding to the period of the TRMM satellite. Polygons indicate the two DYNAMO sounding arrays.

based on the Reynolds et al. (2007) high-resolution (daily,  $0.5^\circ$  horizontal grid) blended analysis. SST fields over the Indian Ocean are from the Woods Hole Oceanographic Institution (WHOI) objectively analyzed air-sea fluxes (OAFlux; daily,  $1^\circ$  horizontal grid) website (<http://oafux.whoi.edu/data.html>) based on Yu and

Weller (2007). Buoy data over the Indian Ocean are from the Research Moored Array for African-Asian-Australian Monsoon Analysis and Prediction (RAMA) provided by the NOAA/Pacific Marine Environmental Laboratory (PMEL) website (<http://www.pmel.noaa.gov/tao/rama/>). Finally, SST data from R/V *Revelle* were

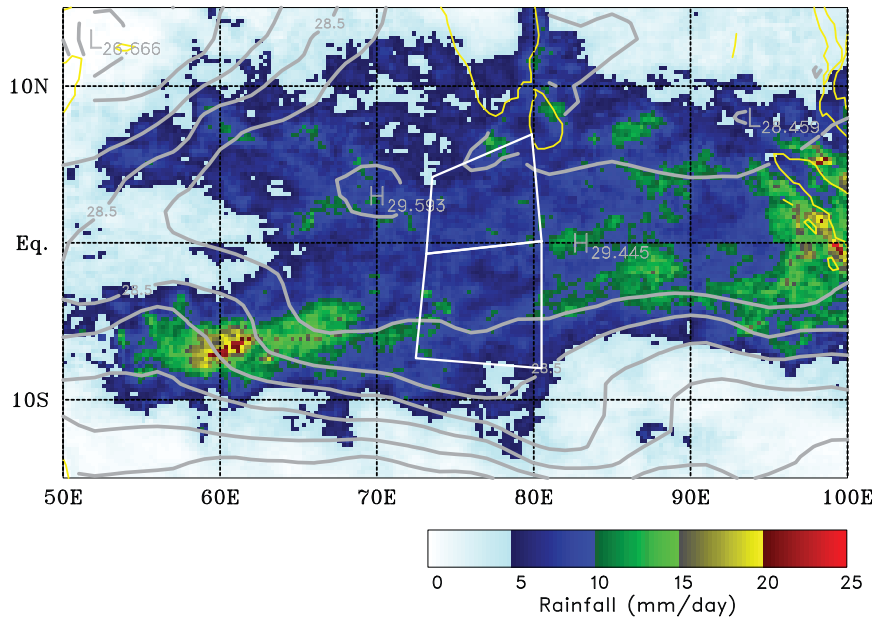


FIG. 4. TRMM 3B42 precipitation ( $\text{mm day}^{-1}$ ) and OAFlux SST ( $^{\circ}\text{C}$ ) for the DYNAMO period 1 Oct–15 Dec 2011. Polygons indicate the two DYNAMO sounding arrays.

made available via <ftp://dynamo.dms.uconn.edu/> through a collaborative effort between NOAA/Physical Sciences Division/ESRL, Oregon State University, and the University of Connecticut.

### c. Analysis procedures

Six-hourly (0000, 0600, 1200, and 1800 UTC) sounding data for the northern and southern arrays, along with P-3 aircraft dropsonde data, were objectively analyzed onto a  $1^{\circ} \times 1^{\circ}$  grid at 25-hPa intervals from 1000 to 50 hPa over the entire domain shown in Fig. 1 using the multiquadric interpolation procedure as described in Ciesielski et al. (1997). Operational global telecommunication system (GTS)-resolution sounding data from sites shown in Fig. 1 outside the arrays were used to help constrain the analyses. Corrections to the divergence were made such that vertical motion balanced to zero at the tropopause level, which was determined at each grid point and time step (Johnson and Ciesielski 2002). However, the divergence profiles presented in the paper are based on the uncorrected values. At this stage, only sounding and aircraft dropsonde data are used in the analyses: at a future time scatterometer winds, profiler winds, and Constellation Observing System for Meteorology Ionosphere and Climate (COSMIC) data will be included.

Thermodynamic and kinematic fields that are presented in the form of time series for the northern and southern arrays are based on daily averaged and spatially averaged values of the interpolated fields over the

respective arrays.<sup>3</sup> Model data are excluded from these array-averaged results; therefore, we emphasize that the time series of fields such as divergence and vertical motion over the arrays are independent of model parameterizations. However, such is not the case for the ECMWF- and NCEP–NCAR-based analyses that are used to provide a larger-scale context for the array results. Those model-based fields are presented 1) for the entire Indian Ocean and 2) in north–south vertical cross sections that extend well beyond the sounding arrays.

### 3. Broad-scale features of the flow and SST

The DYNAMO SOP occurred during La Niña conditions, as reflected by negative SST anomalies over the central and eastern Pacific (Fig. 2). In contrast, the western Pacific and Indian Ocean were characterized by generally positive SST anomalies. This SST anomaly pattern is consistent with the findings of Meyers et al. (2007), who showed that during La Niña conditions, there is an extension of the western Pacific warm pool into the Indian Ocean during a neutral Indian Ocean

<sup>3</sup>The averaging areas for both arrays are kept fixed regardless of ship port calls, although it is recognized that the reliability of the results is diminished during those periods. In recognition of this fact, port-call intervals are denoted in time series plots by shading.

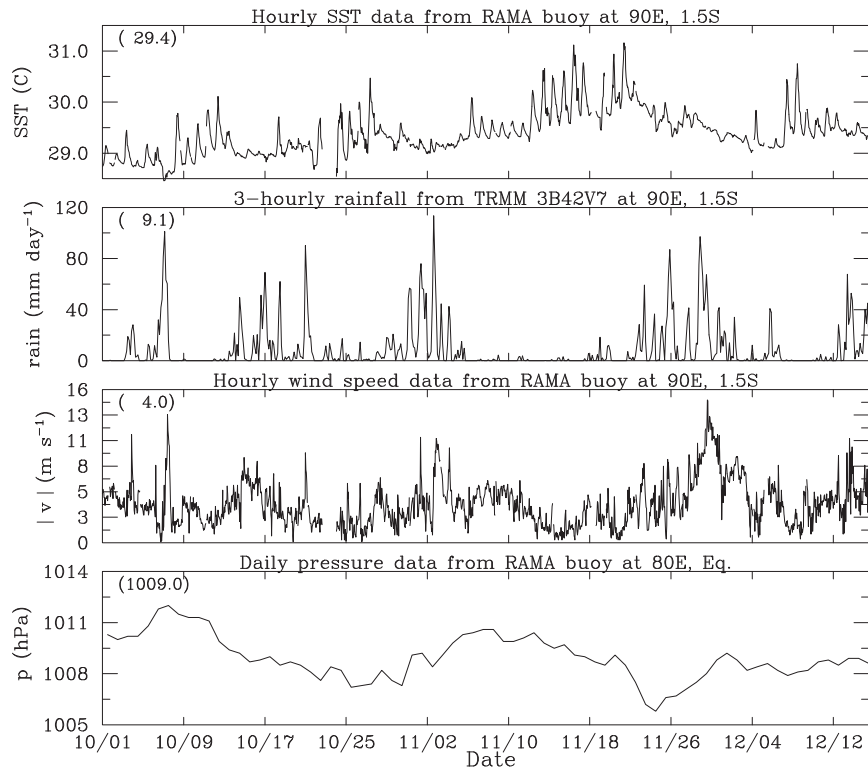


FIG. 5. Time series of (top)–(bottom) hourly sea surface temperature ( $^{\circ}\text{C}$ ) at 1.5-m depth for DYNAMO SOP based on data from the RAMA buoy at  $1.5^{\circ}\text{S}$ ,  $90^{\circ}\text{E}$ , time series of 3-hourly average TRMM 3B42 rainfall ( $\text{mm h}^{-1}$ ) within a  $1^{\circ}$  radius of same buoy, hourly wind speed ( $\text{m s}^{-1}$ ) at same buoy, and time series of daily averaged sea level pressure (hPa) at RAMA buoy at  $0^{\circ}$ ,  $80.5^{\circ}\text{E}$ .

dipole (IOD) state, which existed during the DYNAMO SOP (<http://www.bom.gov.au/climate/enso/indices.shtml>).

SOP-mean TRMM 3B42 rainfall and ECMWF surface streamlines over the Indian Ocean (IO) are shown in Fig. 3a. Two east–west bands of precipitation stretched across most of the IO north and south of the equator, the southern one being most intense. In addition, heavy rainfall occurred along the coast of Sumatra near  $100^{\circ}\text{E}$ . Both precipitation bands were situated along troughs in the surface flow, exhibiting characteristics of intertropical convergence zones (ITCZs). The departure of the rainfall from the 14-yr TRMM 3B42 mean is shown in Fig. 3b, along with the NCEP–NCAR reanalysis 500-hPa vertical motion anomaly field for this same period. Rainfall was slightly above normal over much of the equatorial IO, particularly west of  $70^{\circ}\text{E}$ , although it averaged near the 14-yr mean over the two DYNAMO sounding arrays. The centers of upward (downward) motion from the NCEP–NCAR analysis correspond well to the positive (negative) precipitation anomalies over the IO. The slightly-above-normal precipitation over much of the IO is generally consistent with the anomalously warm SST during the SOP (Fig. 2). The cool SST

anomaly near  $6^{\circ}\text{S}$ ,  $60^{\circ}\text{E}$  is likely related to the substantial rainfall in that vicinity (Fig. 3a).

The SOP-mean SST and precipitation are shown in Fig. 4. While rainfall tended to occur in areas where SST exceeded  $28^{\circ}$ – $29^{\circ}\text{C}$ , the heaviest precipitation was located along the strongest SST gradients. With air flowing from cold to warm water at the northern and southern peripheries of the ITCZ bands (cf. Figs. 3a and 4), boundary layer processes likely played a role in the precipitation development. Specifically, boundary layer growth via enhanced surface fluxes, moistening, and destabilization likely contributed to cloud development and precipitation as air reached the warmer waters nearer the equator (Xie 2004; Small et al. 2008).

While the mean SST was fairly uniform along the equator over much of the IO east of  $60^{\circ}\text{E}$ , there was pronounced SST variability during the SOP associated with the MJOs (Fig. 5). The passage of two MJO active phases, one in late October and another in late November, is evidenced by maxima in rainfall, increases in surface zonal wind speed, and drops in sea level pressure of 4–5 hPa. The SST time series from the RAMA buoy at  $1.5^{\circ}\text{S}$ ,  $90^{\circ}\text{E}$  shows a general warming trend until late

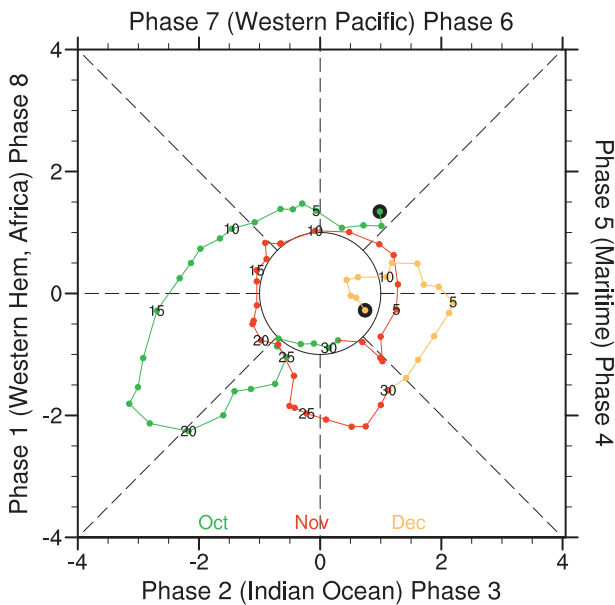


FIG. 6. Wheeler and Hendon (2004) RMM index for the period 1 Oct–15 Dec 2011 illustrating global progression and amplitude of October and November MJOs.

November, followed by cooling into early December. This overall pattern was modulated by distinct intraseasonal variability associated with the October and November MJOs, specifically warming over several-week periods, followed by sharp cooling during rainy, windy periods. This behavior closely resembles the intraseasonal SST variability reported by Vialard et al. (2009) in the Seychelles–Chagos thermocline ridge region of the IO. Brief periods of cooling were also observed during other rainy periods, particularly during the first 3 weeks of October. The other conspicuous feature of the SST time series is the large-amplitude diurnal cycle during the warming and light-wind, light-precipitation periods in October, November, and early December. The damping of the SST diurnal cycle during windy, rainy periods was also observed during TOGA COARE, where it was attributed to wind-induced upper-ocean mixing, cloud shading, and precipitation (Webster et al. 1996). This behavior of the SST in relation to the MJO is very similar to that observed in TOGA COARE (Weller and Anderson 1996; Johnson et al. 1999).

#### 4. Multiscale variability of mean flow properties and rainfall

##### a. Evolution of precipitation features over the Indian Ocean

A time series of the phase and amplitude of the October and November MJOs is shown in Fig. 6 in the

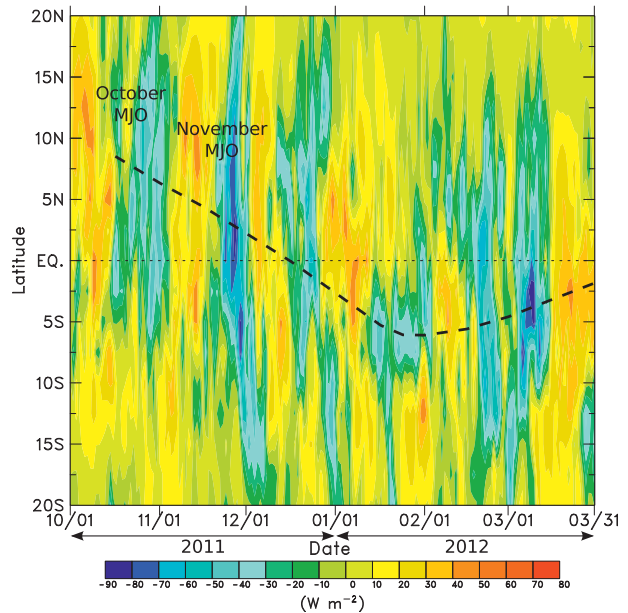


FIG. 7. Time–latitude plot of OLR anomalies ( $\text{W m}^{-2}$ ) computed from the 1981–2010 long-term mean from  $20^{\circ}\text{N}$  to  $20^{\circ}\text{S}$  averaged from  $60^{\circ}$  to  $90^{\circ}\text{E}$  for the period 1 Oct 2011–31 Mar 2012. Approximate seasonal track of anomaly centroid centers is indicated (dashed). October and November MJO active phases are denoted.

form of the Wheeler and Hendon (2004) real-time multivariate MJO (RMM) index for the period 1 October–15 December. Although propagating modes other than the MJO can affect the RMM index (Roundy et al. 2009),

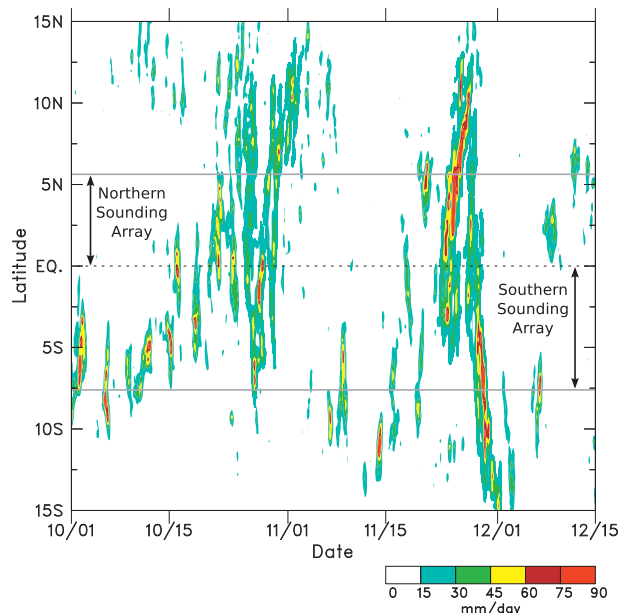


FIG. 8. Time–latitude plot of TRMM 3B42 precipitation ( $\text{mm day}^{-1}$ ) from  $15^{\circ}\text{N}$  to  $15^{\circ}\text{S}$  averaged from  $72^{\circ}$  to  $80^{\circ}\text{E}$  for the period 1 Oct–15 Dec 2011. Latitudinal extents of northern and southern sounding arrays are indicated.

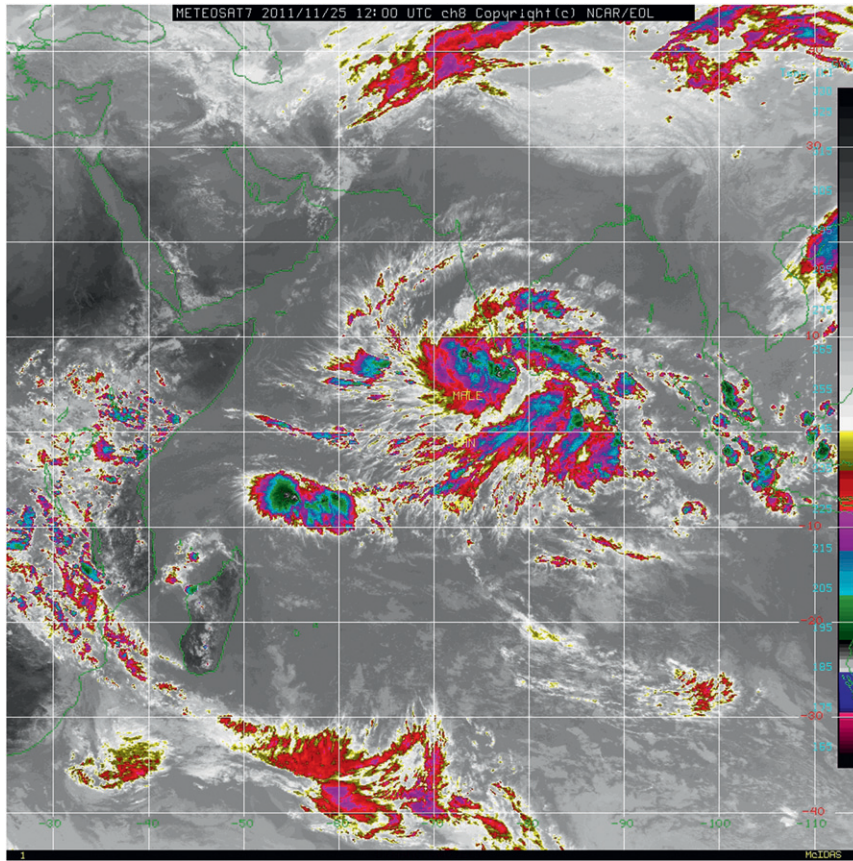


FIG. 9. Meteosat thermal IR image at 1200 UTC 25 Nov 2011. The tropical depression near the southern tip of India became Tropical Storm 05A on 26 Nov.

it is used here to describe the broad-scale view of the MJO events during DYNAMO. The RMM index indicates that both MJOs were at least of moderate amplitude over portions of the Indian Ocean and appear to have completed global circuits—that is, were “successive” events according to the terminology of Matthews (2008).<sup>4</sup> The period between the two MJO events was relatively short ( $\sim 30$  days). This short period is perhaps related to the fact that La Niña conditions existed in the Pacific, permitting a decoupling of the MJO from deep convection earlier than if neutral or El Niño conditions existed (Tam and Lau 2005), hence contributing to a faster global circuit.

<sup>4</sup>Recent work by Straub (2013) indicates that many MJO events that do not appear to be successive in the global-scale RMM index [i.e., appear to develop in situ over the Indian Ocean and are labeled “primary” by Matthews (2008)] do actually have predecessor, eastward-propagating signals of smaller zonal scale that precede the local amplification of the RMM index over the Indian Ocean.

Both MJO events occurred during the period of the seasonal migration of convection from the Northern to Southern Hemisphere, as indicated by a time–latitude plot of OLR anomalies over the central IO from 1 October 2011 to 31 March 2012 (Fig. 7). The largest OLR anomalies during the October–November period occurred north of the equator; hence, the northern sounding array captured the strongest convective signal of the MJOs. The depiction in Fig. 7 is expanded in a time–latitude plot of TRMM 3B42 precipitation averaged over the longitudes of the sounding arrays (Fig. 8). Over the northern array, which extends approximately from the equator to  $5^{\circ}\text{N}$  (Fig. 1), very little precipitation occurred outside the active periods of the October and November MJOs, whereas the southern array (extending approximately from the equator to  $7.5^{\circ}\text{S}$ ) experienced relatively frequent episodes of precipitation. Figure 8 also reveals that the behavior of the precipitation during the two MJOs was quite different, with the October event characterized by a series of 2-day near-equatorial maxima, much like the December 1992 MJO during TOGA COARE (Takayabu et al. 1996; Haertel and Johnson

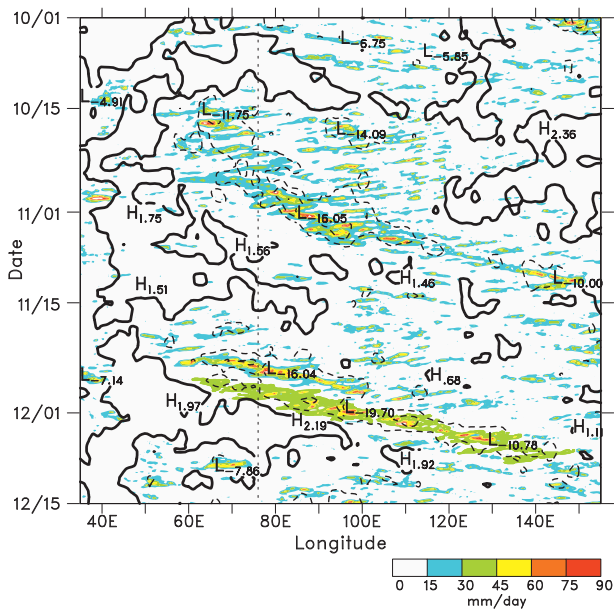


FIG. 10. Time-longitude plot of TRMM 3B42 precipitation ( $\text{mm day}^{-1}$ ) and ECMWF 500-hPa vertical  $p$  velocity ( $\text{hPa h}^{-1}$ ) from  $35^{\circ}$  to  $155^{\circ}\text{E}$  averaged from  $5^{\circ}\text{N}$  to  $5^{\circ}\text{S}$  for the period 1 Oct–15 Dec 2011. Thick solid line is the zero contour; dashed contours indicate upward motion with a contour interval of  $10 \text{ hPa h}^{-1}$ . Vertical dashed line denotes the center of DYNAMO sounding arrays.

1998), while the November MJO was dominated by two strong precipitation events. The latter two features were designated Kelvin waves by the real-time filtering technique of Wheeler and Weickmann (2001) applied to OLR data ([http://cawcr.gov.au/staff/mwheeler/maproom/OLR\\_modes/index.htm](http://cawcr.gov.au/staff/mwheeler/maproom/OLR_modes/index.htm)). In addition, the prominent precipitation signals migrating poleward are indications of Rossby gyres associated with the November equatorial convection (Gill 1980), as also observed during TOGA COARE (Chen et al. 1996). An infrared satellite image on 25 November (Fig. 9) shows the northern circulation feature, which became Tropical Storm 05A near the southern tip of India on 26 November and subsequently moved into the Arabian Sea. While the two precipitation signals have characteristics of Kelvin waves, their relatively slow speed ( $\sim 8 \text{ m s}^{-1}$ ) and the existence of associated trailing poleward-moving low-level cyclones may place these events on the continuum between the MJO and Kelvin waves described by Roundy (2012b).

A time-longitude plot of the TRMM 3B42 rainfall (Fig. 10) along with ECMWF 500-hPa vertical motion depicts the two MJO convective envelopes, each consisting of both eastward and westward disturbances—common features of MJOs (Nakazawa 1988). A diurnal cycle of westward-moving precipitation features is observed over the longitudes of Borneo and Sumatra ( $100^{\circ}$ – $120^{\circ}\text{E}$ ),

which is consistent with the findings of Mori et al. (2004) and Sakurai et al. (2005). In October, the diurnal cycle transitioned to a quasi-2-day cycle farther west near the longitudes of the DYNAMO sounding arrays. In November, a 2-day cycle near the DYNAMO array was less prominent; rather, the behavior was dominated by two long-lived precipitation events. To the west, precipitation associated with each MJO appeared to first develop near the longitudes  $50^{\circ}$ – $60^{\circ}\text{E}$ , where the SST began to exceed  $28.5^{\circ}\text{C}$  (Fig. 4). The agreement between the ECMWF vertical motion field and precipitation is quite good, not only over the longitudes of the DYNAMO arrays where sounding data from multiple sites have been assimilated into the operational system, but elsewhere throughout the domain.

### b. Contrast of wind and thermodynamic properties over northern and southern sounding arrays

Time series of zonal wind, relative humidity (with respect to ice for  $T < 0$ ), perturbation temperature, and precipitation averaged over the northern sounding are shown in Fig. 11. The rainfall time series clearly indicates the passage of the MJO active phases during the latter half of October and November. A 2-day periodicity of rainfall is evident for the October MJO, whereas the November event is dominated by a 4–5-day cycle of precipitation. A gradual buildup in lower-tropospheric moisture over 1–2-week periods is observed for both MJOs starting during the second weeks of October and November, followed by more rapid moistening of the mid- to upper troposphere just after the middle of each month. Rapid drying in the lower troposphere occurred toward the end of the precipitation episodes along with increased westerlies, as found during TOGA COARE (Lin and Johnson 1996). Enhanced easterlies developed aloft during and immediately following the MJO active phases, with the wind speed maxima shifting downward with time. A similar downward tilt is seen in the temperature anomaly pattern between 50 and 200 hPa, particularly for the November MJO. The descent of the cold anomalies leads to a corresponding descent of the cold-point tropopause, followed by a sudden upward jump at the end of the heavy-rain period (illustrated in a schematic depiction at the end of the paper). This tilted temperature anomaly structure near the tropopause was first noted by Kiladis et al. (2001), who explained the feature as a gravity-wave response to the MJO convective heat-source envelope.<sup>5</sup> More recently, it has been found that this phenomenon is also manifested in CALIPSO cirrus

<sup>5</sup> The same feature is also observed in convectively coupled Kelvin waves in the eastern Pacific studied by Straub and Kiladis (2002).

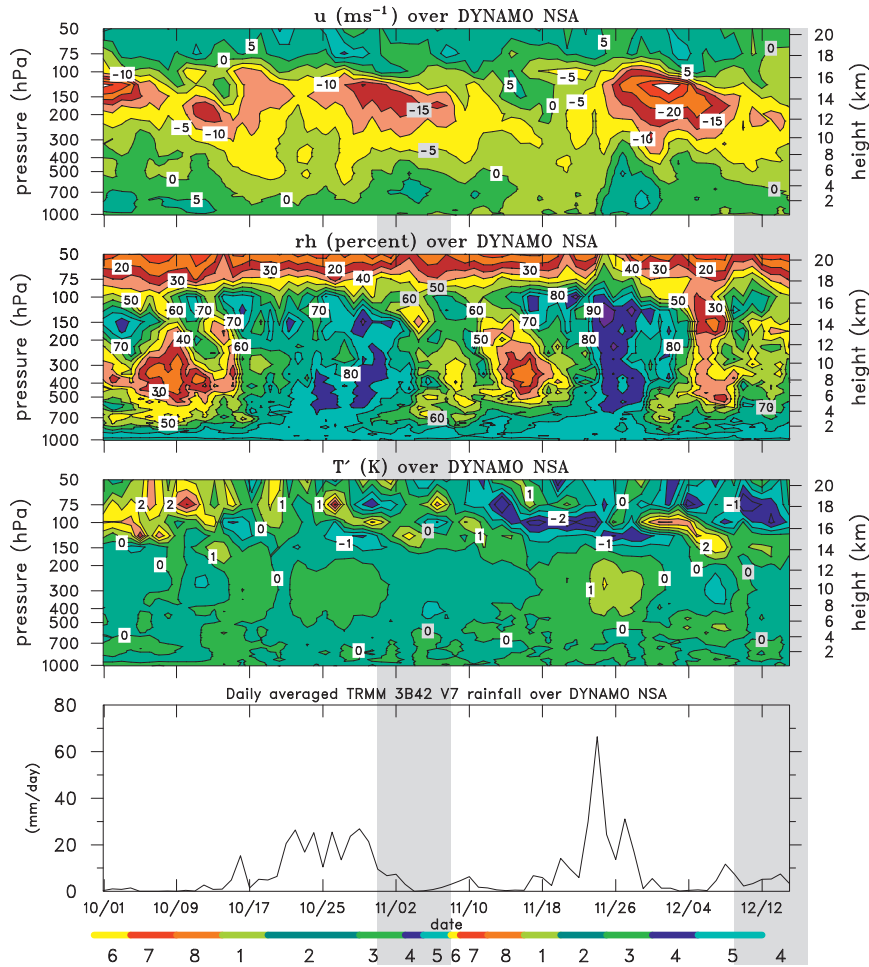


FIG. 11. Time series over the northern sounding array of (top)–(bottom) zonal wind ( $\text{m s}^{-1}$ ), relative humidity (%; with respect to ice for  $T < 0^\circ\text{C}$ ), temperature anomaly ( $^\circ\text{C}$ ), and daily averaged TRMM 3B42 rainfall ( $\text{mm day}^{-1}$ ). Winds and thermodynamics are based on daily averages of 6-hourly soundings, with the temperature anomaly based on the SOP mean. Colored bars at bottom refer to phases of RMM index shown in Fig. 6. Vertical shaded bars indicate times when R/V *Revelle* was off station.

data (Virts and Wallace 2010; Virts et al. 2010). These authors found that the coldest, cloudiest anomalies aloft occurred  $30^\circ$  to the east of main MJO convective heat source and descend with time, which is qualitatively consistent with the temperature anomalies near the tropopause observed during DYNAMO. The correspondence between the cool and moist anomalies aloft ( $\sim 100\text{--}200$  hPa) preceding the heaviest rainfall can also be seen for the October and November MJOs. The overall upper-tropospheric temperature anomaly pattern, particularly for the November MJO, characterized by a warm anomaly centered near 300 hPa and cold/warm tilted anomalies at and above the tropopause, closely resembles the reanalysis-based MJO structure deduced by Kiladis et al. (2005, their Fig. 7). Weak cool

anomalies are observed near the surface in association with precipitation and associated convective downdrafts.

The time series of zonal wind, relative humidity, and precipitation averaged over the southern array is shown in Fig. 12. While evidence of the two MJOs can be seen in all fields, the strength of the moisture signal (relative humidity and precipitation) is somewhat weaker than over the northern array. Particularly noteworthy is the lack of a distinct buildup of low-level moisture prior to the periods of heaviest precipitation in late October and November. In addition, frequent periods of midtropospheric moistening are observed throughout the SOP, providing further evidence that the southern array straddled a relatively persistent ITCZ trough (Fig. 3a) with somewhat less modulation by MJO passage (Fig. 7).

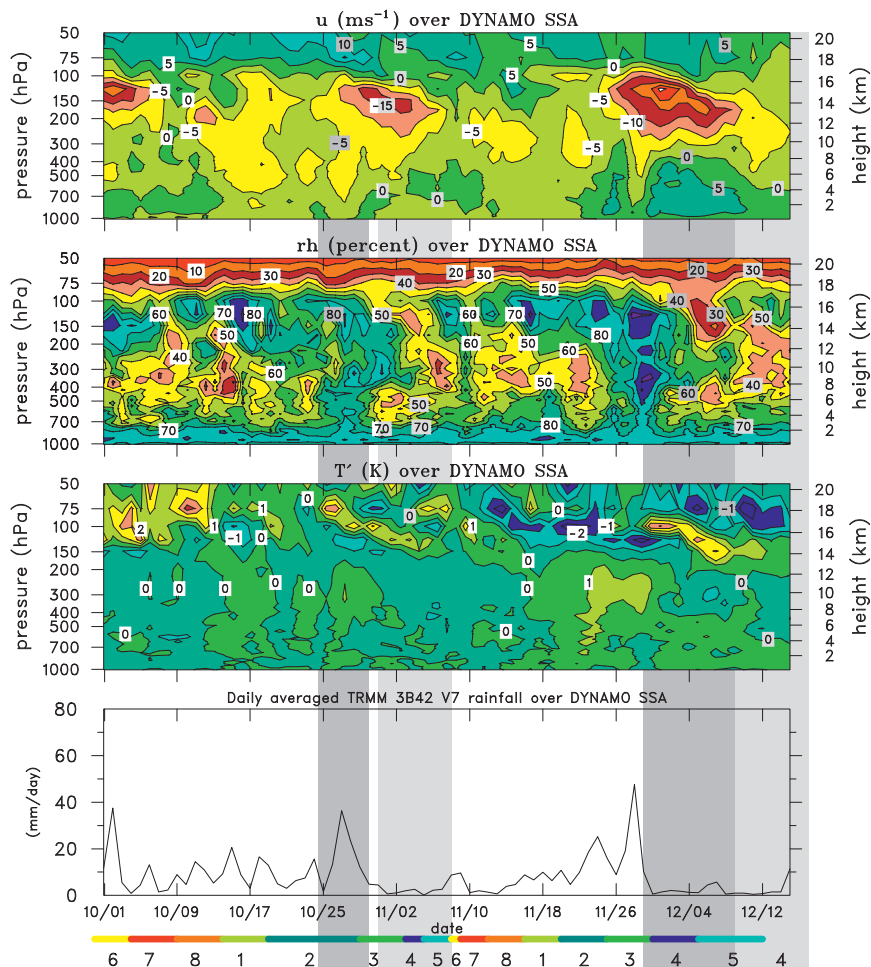


FIG. 12. As in Fig. 11, but for the southern sounding array. Dark and light vertical shaded bars indicate times when R/V *Mirai* and *Revelle*, respectively, were off station.

The time series shown in Figs. 11 and 12 are based on daily averaged fields. Relative humidity time series at four stations based on the full resolution of the sounding data (3 hourly at Gan Island, R/V *Revelle*, and Diego Garcia; 6 hourly at Malé) are shown in Fig. 13. A striking feature is the distinct difference between the time series at Diego Garcia at 7.3°S and those near the equator (Gan Island and *Revelle*) and to the north (Malé), indicating a weaker signal of intraseasonal variability to the south. In addition, the higher-resolution data reveal moistening episodes at all sites on time scales ranging from diurnal to 4–5 days to intraseasonal. Particularly noteworthy are 2-day oscillations in mid-October and 4–5-day disturbances in mid- to late November at the northern-array sites, consistent with the precipitation time series (Fig. 11). Moreover, at Malé (4.2°N), Gan, and *Revelle*, a stepwise progression of the moistening is evident. In particular, during the October MJO, moist conditions were primarily confined below 800–850 hPa

for the first 10–15 days of the month, suggestive of trade wind–like cumulus conditions as observed episodically during TOGA COARE (Johnson and Lin 1997). This period is followed by an approximately 1-week-long interval of moistening to the midtroposphere (~500 hPa), although the onset of this period is about 5 days later at Malé, and then by moistening through the entire troposphere. The period of deep moistening is interrupted by drying episodes on a 2-day time scale. Figure 13 also indicates a similar sequence of events in November, apart from the data gaps at *Revelle*, as well as during a December MJO-like event not studied here. This stepwise pattern of moistening in association with MJO passage was also noted by Kikuchi and Takayabu (2004) over Indonesia during TOGA COARE and by Yoneyama et al. (2008) during MISMO. Also present at Malé and Gan are descending dry anomalies near the tropopause, which are associated with the descending warm anomalies over the northern sounding array (NSA) (Fig. 11).

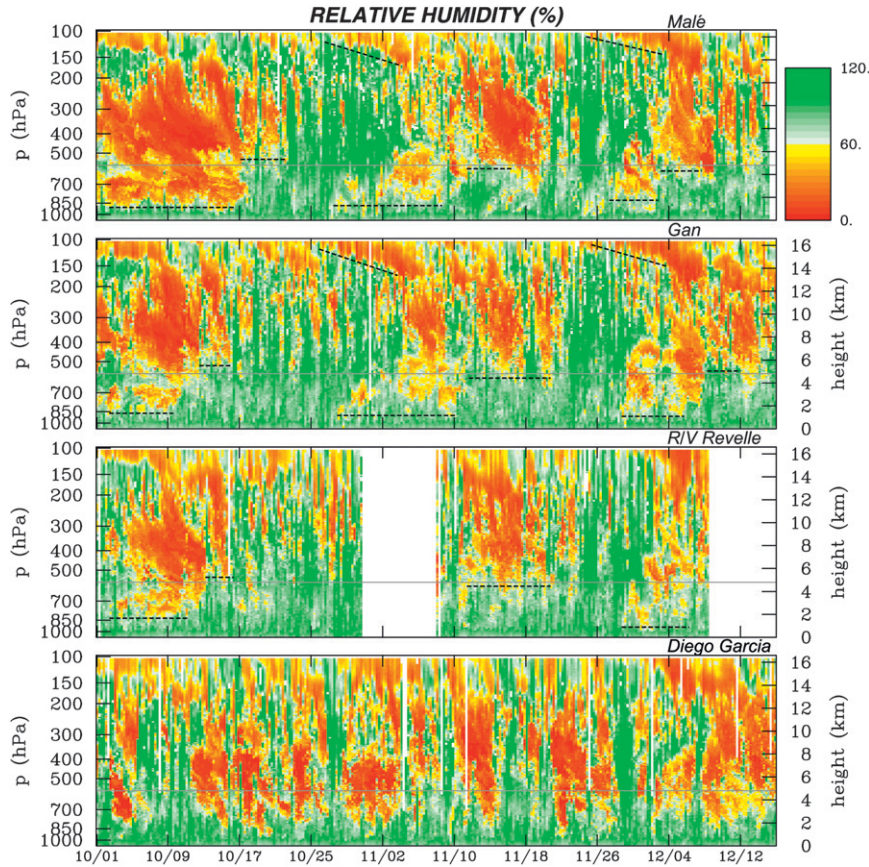


FIG. 13. Time series of relative humidity (%; with respect to ice for  $T < 0^{\circ}\text{C}$ ) from 1 Oct to 15 Dec at Malé, Gan Island, R/V *Reville*, and Diego Garcia based on full time resolution of sounding data. See Fig. 1 for site locations. Dotted line segments denote approximate tops of moist layers. Thin gray line denotes  $0^{\circ}\text{C}$  level.

A comparison of the vertical profiles of the mean flow and thermodynamic properties over the two sounding arrays is shown in Fig. 14 covering the period 1 October–30 November when the arrays were most complete. Low-level westerlies and upper-level easterlies, and hence the mid-to-upper-level shear, were stronger in the northern array. Low-level southerlies and upper-level northerlies were present over both the northern and southern arrays (though stronger to the south), likely an indication of the weakening, yet still present, Asian summer monsoon circulation. Profiles of equivalent potential temperature were similar between the two arrays, while the midtroposphere over the northern array was slightly moister, as also evident by comparing Figs. 11 and 12. The greatest variability in  $\theta_e$  and relative humidity was in the mid- to upper troposphere associated with the passage of the MJOs, consistent with Yuan and Houze (2013), being somewhat greater over the northern array.

Changes in the zonal wind and relative humidity at Gan Island from the preactive to active phases of the

October and November MJOs are shown in Fig. 15. The times for the preactive and active profiles were selected based on driest and moistest midlevel conditions in the respective months, so the full amplitude of the mid-tropospheric moistening is emphasized. The most notable relative humidity change is the substantial moistening in the mid- to upper troposphere, increasing from a minimum around 20% near 300 hPa to nearly saturated conditions in the latter part of both months. Unlike the October MJO, the November event did not show much change in the low-level moisture (below 600 hPa) from the preactive to active phase. In October (Fig. 15, top-right panel), the low-level zonal flow was similar during both periods owing to the fairly strong westerlies early in the month (Fig. 11). Upper-level easterlies were also moderately strong in early October, so there was not a marked change from the first to the last half of the month. However, in November there was a prominent shift in the zonal winds from light easterly at low levels early in the month to strong westerlies later (Fig. 15,

Basic fields for 01 Oct – 30 Nov 2011

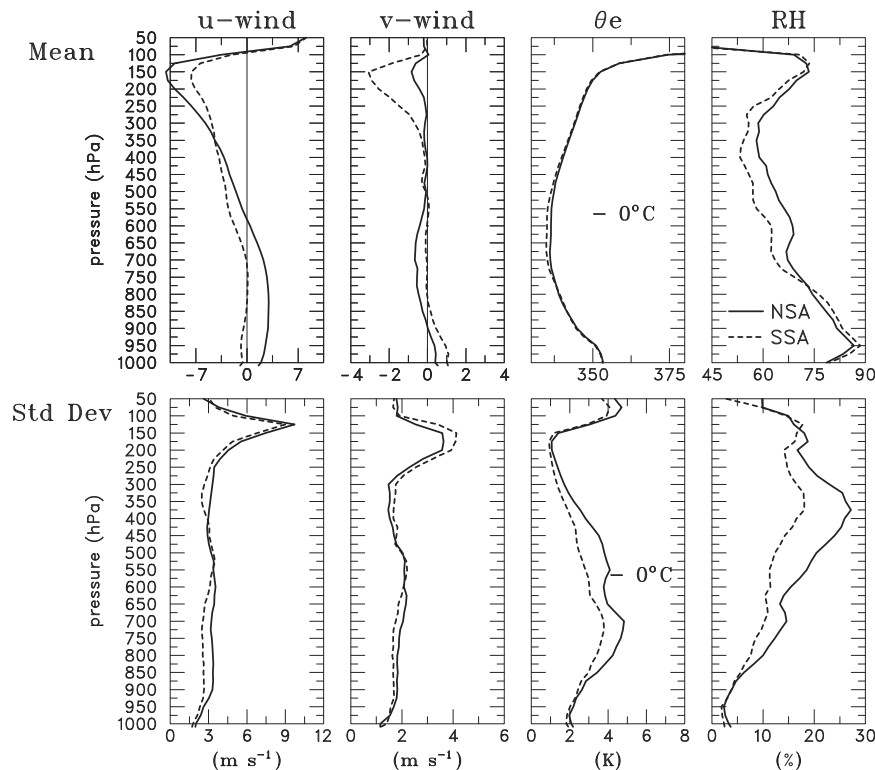


FIG. 14. (top) Two-month (1 Oct–30 Nov) mean vertical profiles of zonal and meridional wind ( $\text{m s}^{-1}$ ), equivalent potential temperature (K), and relative humidity (%; with respect to ice for  $T < 0^\circ\text{C}$ ), and (bottom) standard deviations of these variables for the northern (solid) and southern (dashed) sounding arrays.

bottom-left panel). In addition, there was a marked development of easterlies aloft between 100 and 150 hPa with the passage of the active phase of the MJO. The shear profile during the November active phase resembles that observed during the convectively active phase of MISO. Yamada et al. (2010) hypothesized that the easterly shear during MISO led to westward-moving cloud shields (advected by easterlies aloft) that interacted with eastward-moving convective disturbances to produce a 2–4-day cycle of convection within the larger-scale convective envelope of the eastward-moving MJO. The extent to which this convective behavior occurred during DYNAMO is yet to be determined.

The changing north–south properties of the flow from the first to the second half of October are shown in Fig. 16. To obtain a broader latitudinal perspective than just the sounding arrays, these plots are based on the ECMWF operational analyses. The areas north and south of the sounding arrays are essentially devoid of reliable sounding data (stations in India contain numerous errors), so we utilize the ECMWF product for this broader view. As noted earlier, the ECMWF analyses from  $5^\circ\text{N}$

to  $10^\circ\text{S}$  agree well with those based on the sounding data alone. During the first half of the month (Fig. 16, left panel), two rainfall bands were evident north and south of the equator, although the northern one between  $10^\circ$  and  $15^\circ\text{N}$  was relatively weak. Strongest low-level convergence of the meridional flow and divergence aloft was coincident with the rainfall maximum near  $5^\circ\text{S}$ . A marked change occurred during the last half of October (Fig. 16, right panel). The rainfall maximum shifted to the equator with considerable precipitation extending well north of the equator. The mid- to upper troposphere moistened considerably at this time. Very little convergence of the meridional flow was present in the vicinity of the equator in the latter half of October, suggesting that the primary contributor to low-level convergence at that time was associated with the zonal flow (to be discussed later). The centroid of heavy rainfall in late October was north of the equator, but the strongest meridional flow was in the opposite hemisphere. This feature is consistent with Hack et al. (1989) and Schubert et al. (1991), who showed that this asymmetric response of the meridional circulation to heating is due to the anisotropy

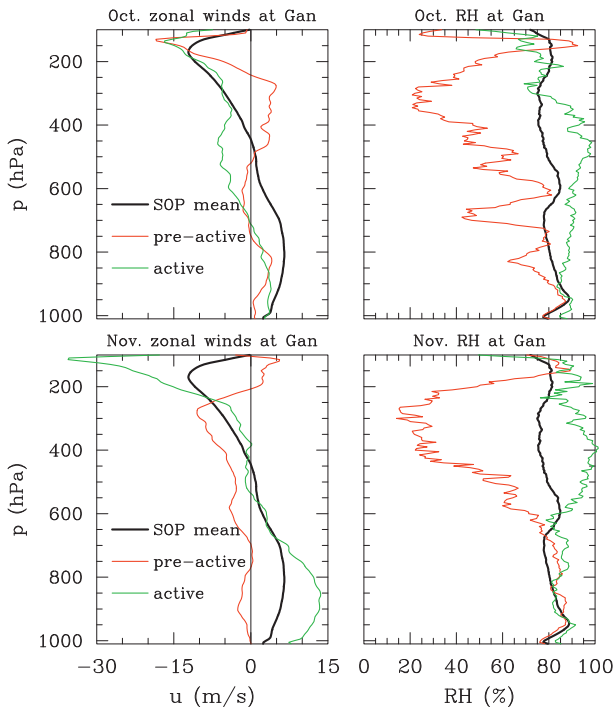


FIG. 15. Mean, preactive, and active phase profiles of (left) zonal wind ( $\text{m s}^{-1}$ ) and (right) relative humidity (%; with respect to ice for  $T < 0^\circ\text{C}$ ) for (top) October and (bottom) November. Preactive and active dates are 5 and 26 October and 16 and 27 November.

associated with the spatial variation of the inertial stability field; that is, the low inertial stability in the equatorial region facilitates a stronger meridional circulation on the equatorward side of the main heated region. Their results assume zonal symmetry (i.e., no east–west circulations such as those associated with the MJO); however, they might be expected to qualitatively apply to the findings here.

A similar shift from a double ITCZ to a broad rainfall maximum near the equator was seen during the passage of the November MJO (Fig. 17). In this case, the rainfall was fairly evenly distributed across the equator during the active phase, as was the diverging outflow aloft. This result, too, is consistent with Hack et al. (1989), who showed a symmetric response of the upper-level outflow with a heat source on the equator. However, there was an off-equatorial center of maximum convergence of the low-level meridional flow (near  $3^\circ\text{N}$ ). This feature is likely related to the tropical cyclone activity in the Northern Hemisphere associated with the November MJO (Fig. 9).

### 5. Diagnosed divergence and vertical motion

The evolution of divergence (uncorrected) and vertical motion over the northern sounding array is shown in

Fig. 18. Enhanced low-level convergence, upper-level divergence, and upward motion were observed during the active phases of each MJO, although a longer period of deep convection inferred from these fields occurred with the October event. This finding is consistent with the approximately 3-week period of midtropospheric moistening in October (Fig. 11). Low-level convergence, divergence aloft, and upward vertical motion progressively deepened with time in October, suggesting an evolution from shallow cumulus and congestus to deep convection with this event, as indicated by past studies (Johnson et al. 1999; Kikuchi and Takayabu 2004; Mapes et al. 2006; Yoneyama et al. 2008; Del Genio et al. 2012). A similar progression is seen during the buildup phase in November, but it is briefer, less distinct, and characterized by a more abrupt onset to deep, vigorous upward motion. Consistent with evolution of zonal wind, temperature, and moisture anomalies during the active phases of each MJO (Fig. 11), there is a descent with time of the altitude of the peak upper-level divergence.

Time series of divergence and vertical motion for the southern array (Fig. 19) show a distinct contrast with those for the northern array (Fig. 18). Although evidence of enhanced low-level convergence, upper-level divergence, and upward motion occurred in late October and November, there were more frequent periods of upward motion throughout the entire SOP. This behavior is consistent with the time series of relative humidity (Fig. 12) showing frequent periods of moistening, thus reinforcing the picture of quasi-persistent ITCZ conditions south of the equator.

As just seen, the evolution of divergence and vertical motion differed significantly between the two arrays. The 1 October–30 November mean profiles of these fields, while broadly similar, also exhibited notable differences (Fig. 20). A deep layer of lower-tropospheric convergence occurred within both arrays with divergence aloft in the 100–300-hPa layer. However, the layer of convergence was deeper over the northern array, extending above the  $0^\circ\text{C}$  level. This feature is possibly an indication of a somewhat higher percentage of stratiform precipitation and, hence, melting-layer convergence (Mapes and Houze 1995), north of the equator where the MJO signal was greatest. This supposition is yet to be confirmed by independent measurements but is consistent with the finding by Lin et al. (2004) of a greater fraction of stratiform rainfall within MJO convection than the global tropical mean. The amplitudes of the mean vertical motion profiles for the two arrays were quite similar, consistent with the approximately equal TRMM-estimated rainfall rates  $7.8$  and  $8.0 \text{ mm day}^{-1}$  for the northern and southern arrays, respectively. However, the vertical motion over the northern array had a distinct

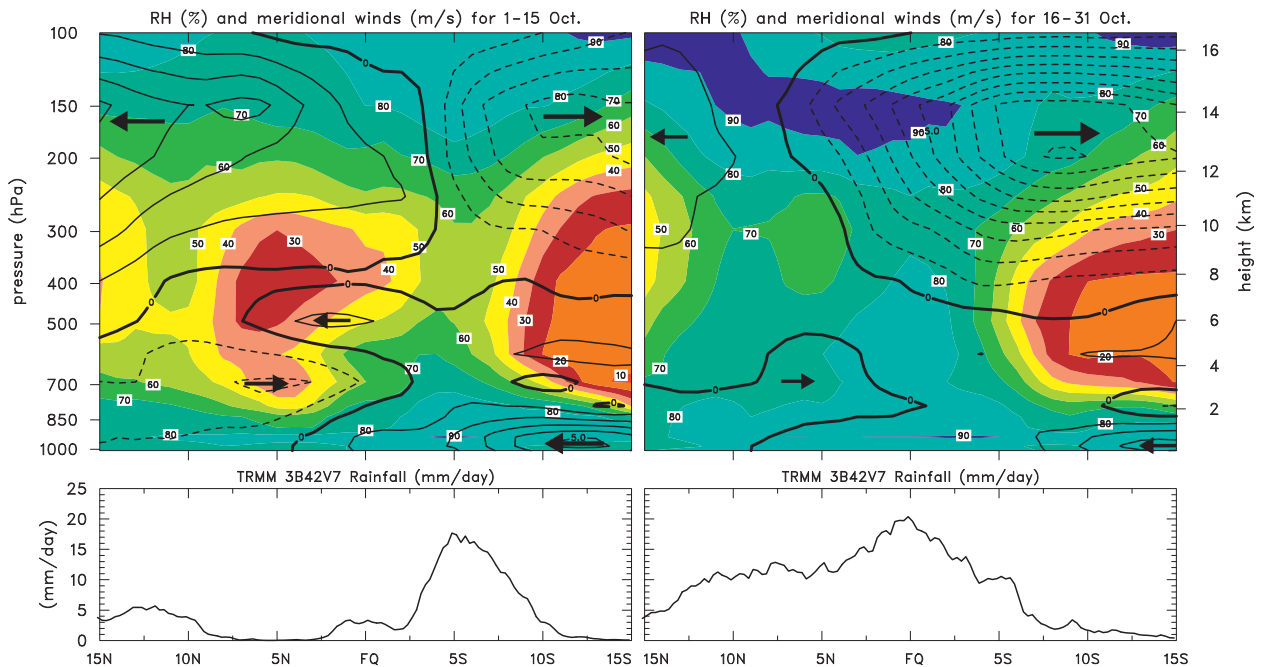


FIG. 16. North–south cross section through sounding arrays of ECMWF operational analysis (top) relative humidity (%; shading; with respect to ice for  $T < 0^{\circ}\text{C}$ ) and meridional wind (contour interval =  $1\text{ m s}^{-1}$ ) and (bottom) TRMM 3B42 rainfall for periods (left) 1–15 Oct and (right) 16–31 Oct 2011.

peak in the upper troposphere (between 350 and 400 hPa) whereas the vertical motion over the southern array had a broader peak with a weak maximum near 550 hPa, suggesting differing characteristics of convection between the

two domains. The more-elevated peak to the north is also indicative of a higher fraction of stratiform rainfall in that region compared to the south (Houze 1982; Johnson 1984; Houze 1989; Schumacher et al. 2004). Further analysis of

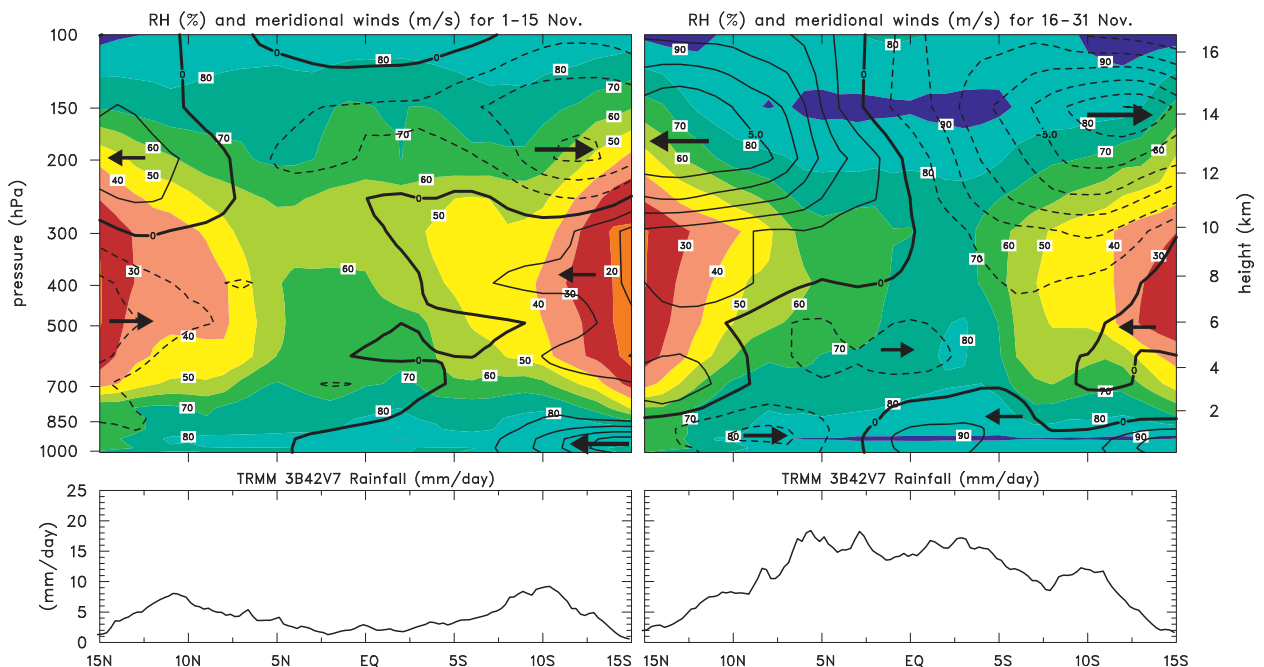


FIG. 17. As in Fig. 16, but for periods (left) 1–15 Nov and (right) 16–30 Nov 2011.

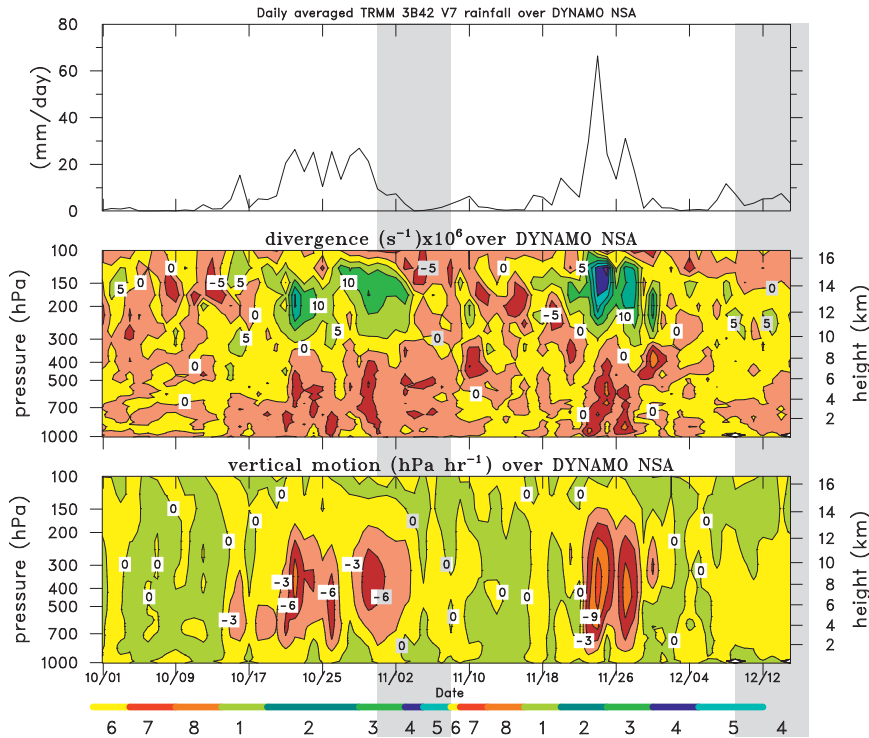


FIG. 18. SOP time series of (top) TRMM 3B42 rainfall, (middle) uncorrected divergence ( $10^{-6} \text{ s}^{-1}$ ), and (bottom) vertical motion ( $\text{hPa h}^{-1}$ ) for the northern sounding array. Colored bars at bottom refer to phases of RMM index shown in Fig. 6. Vertical shaded bars indicate times when R/V *Reville* was off station.

these differences is underway based on computations of heat and moisture budgets.

North–south vertical cross sections of horizontal divergence, relative humidity, and potential temperature from the ECMWF operational analyses, along with TRMM 3B42 rainfall for the first and second halves of October are shown in Fig. 21. The transition from a double-ITCZ structure to a single, broad rain maximum along the equator is accompanied by a similar shift of the low-level convergence–upper-level divergence patterns. The relatively shallow low-level convergence layer in the rainbands in early October transitioned to a deep layer of convergence extending to 400 hPa during the latter half of the month. The existence of low-level convergence at and near the equator in the last half of October but with negligible convergence of the meridional flow (Fig. 16) suggests that the primary contributor to convergence at this time was in the zonal flow, consistent with the expectations for a Kelvin–Rossby wave response to an equatorial heat source Gill (1980).

A similar transition occurred from the first to the second half of November when there was a shift from a double-ITCZ pattern to a broad rainfall maximum along the equator (Fig. 22). A deeper layer of lower-tropospheric convergence occurred in the latter half of November

along with stronger, more-elevated peaks in upper-level divergence. A convergence maximum near 500 hPa in late November is once again suggestive of melting-layer effects in association with stratiform precipitation during the active phase of the MJO. Both the mean divergence profiles based on sounding data only (Fig. 20) and those from the ECMWF analysis (Figs. 21 and 22) indicate a slightly higher level of the peak in upper-level divergence over the northern array than the southern array. This behavior could be related to the slightly higher average SSTs over the northern array (Fig. 4) during the SOP and/or the predominance of the MJO signal to the north accompanied by more organized convection.

Vertical cross sections of vertical motion for the first and last halves of November are presented in Fig. 23. Over this period, there is a shift in the level of the peak upward motion from the low to midtroposphere to the mid- to upper troposphere. The higher peak during late November is consistent with the earlier inference of a higher percentage of stratiform precipitation during the active phase of the MJO. A similar broadening, intensification, and high-level peak (near 400 hPa) in upward motion occurred during the late-October active phase of the MJO (not shown).

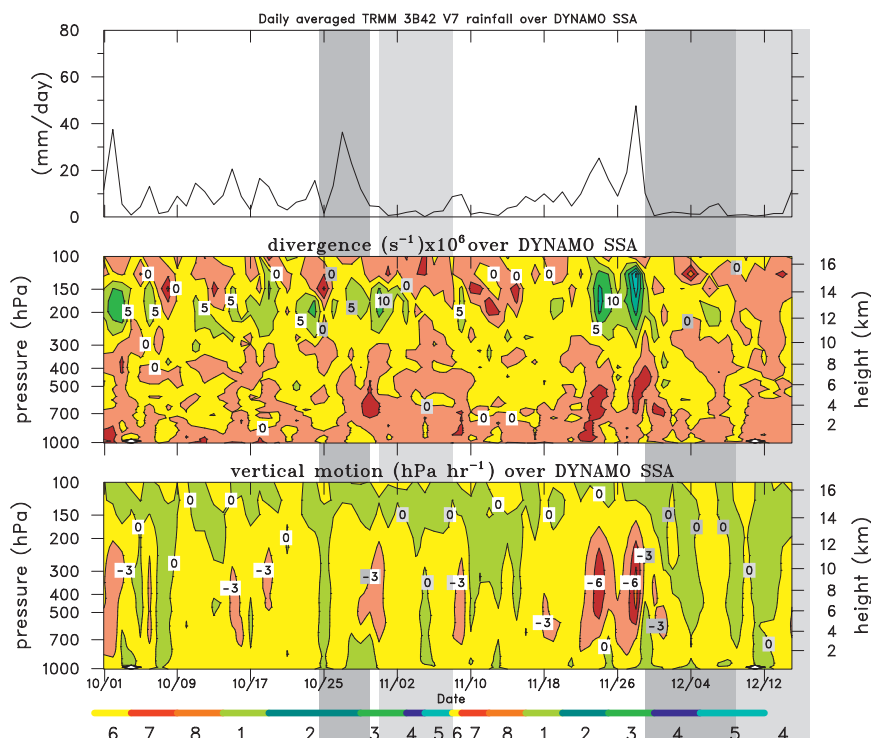


FIG. 19. As in Fig. 18, but for the southern array. Dark and light vertical shaded bars indicate times when R/V *Mirai* and *Revelle*, respectively, were off station.

## 6. Summary and conclusions

Sounding data from two quadrilateral arrays, one north and one south of the equator, have been used to diagnose the kinematic and thermodynamic properties and structure of the October and November 2011 MJO events during the DYNAMO field campaign over the Indian Ocean. The analyses for the sounding arrays are based on a preliminary version of the quality-controlled, high-resolution sounding dataset. Efforts to complete quality control of the data (e.g., corrections for sonde humidity biases) are ongoing.

The principal findings with respect to the broad-scale conditions during the DYNAMO special observing period over the Indian Ocean are

- DYNAMO occurred during a La Niña and near-neutral Indian Ocean dipole conditions such that positive SST anomalies existed over much of the Indian Ocean; correspondingly, slightly-above-normal precipitation occurred over much of the Indian Ocean.
- The heaviest precipitation over the Indian Ocean occurred in east–west bands north and south of the equator in proximity to the strongest SST gradients.

With respect to the evolution of the winds, vertical motion, thermodynamic fields, SST, and precipitation during the passage of the two MJOs, the primary

findings are summarized in Fig. 24. The northern array experienced the strongest MJO signal, so this schematic depiction refers to results for that domain. Specifically, precipitation over the northern sounding array was strongly modulated by the MJOs; the southern array experienced more persistent, briefer episodes of precipitation mostly related to ITCZ convection.

- The development of the October MJO over the northern sounding array was characterized by gradual moistening of the low to midtroposphere over an approximately 2-week period during which multiple westward-moving, 2-day disturbances affected the region, similar to the December 1992 MJO during TOGA COARE (Takayabu et al. 1996; Haertel and Johnson 1998).
- The November MJO exhibited a similar roughly 2-week period of a buildup of low- to midlevel moisture preceding the convectively active phase, which was dominated by two strong Kelvin waves, each with diagnosed intense upward motion.
- Low-level westerly flow preceded the October MJO; low-level easterlies preceded the second MJO.
- Patterns of relative humidity, divergence and vertical motion support the concept of shallow cumulus-to-congestus-to-deep convection evolution of the cloud population in a stepwise manner, which is consistent

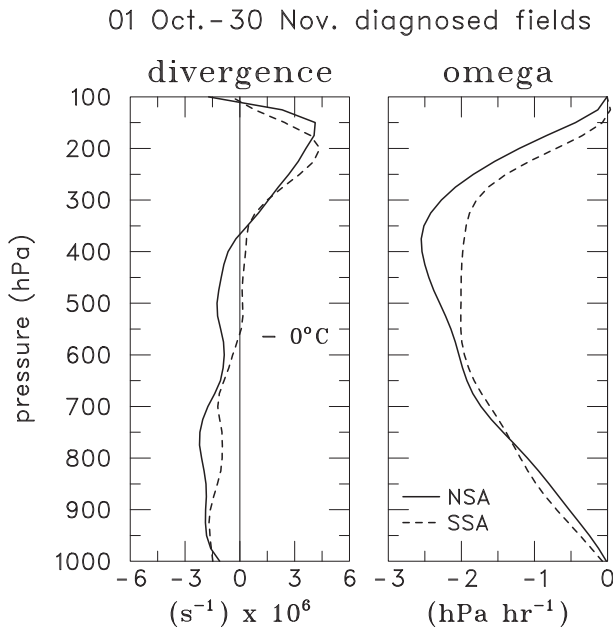


FIG. 20. Mean vertical profiles of (left) divergence ( $10^{-6} \text{ s}^{-1}$ ) and (right) vertical motion ( $\text{hPa h}^{-1}$ ) from 1 Oct to 30 Nov for the northern (solid) and southern (dashed) sounding arrays.

with past studies (Kikuchi and Takayabu 2004; Yoneyama et al. 2008; Del Genio et al. 2012).

- Thermal anomalies in the low to midtroposphere within the MJO convective envelope—cool anomalies

at low levels and warm anomalies in the upper troposphere—are consistent with findings from past studies (Lin and Johnson 1996; Kiladis et al. 2005).

- Tilted cool/warm and zonal wind anomalies occurred for extended periods (multiple weeks) in the upper troposphere and lower stratosphere, reflecting gravity or Kelvin waves excited by the MJO convective envelopes (Kiladis et al. 2001; Virts and Wallace 2010; Virts et al. 2010); the temperature anomalies contributed to sharp jumps in the cold-point tropopause level at the end of the heavy rainfall periods.
- The cool-anomaly portions of these upper-level features had associated positive moisture anomalies aloft that arrived several weeks prior to the heaviest rain periods of the MJOs.
- The quiescent period of the MJOs were characterized by gradual SST rises with accompanying distinct diurnal cycles, while the active phases exhibited falling SSTs with a damped diurnal cycle, as also found during TOGA COARE (Webster et al. 1996; Weller and Anderson 1996).

While there are a number of similarities in the characteristics of the two MJOs, there are sufficient differences to warrant caution in generalizing results from these events. In particular, we attempted the creation of a composite of the two cases by RMM phase, but it led to

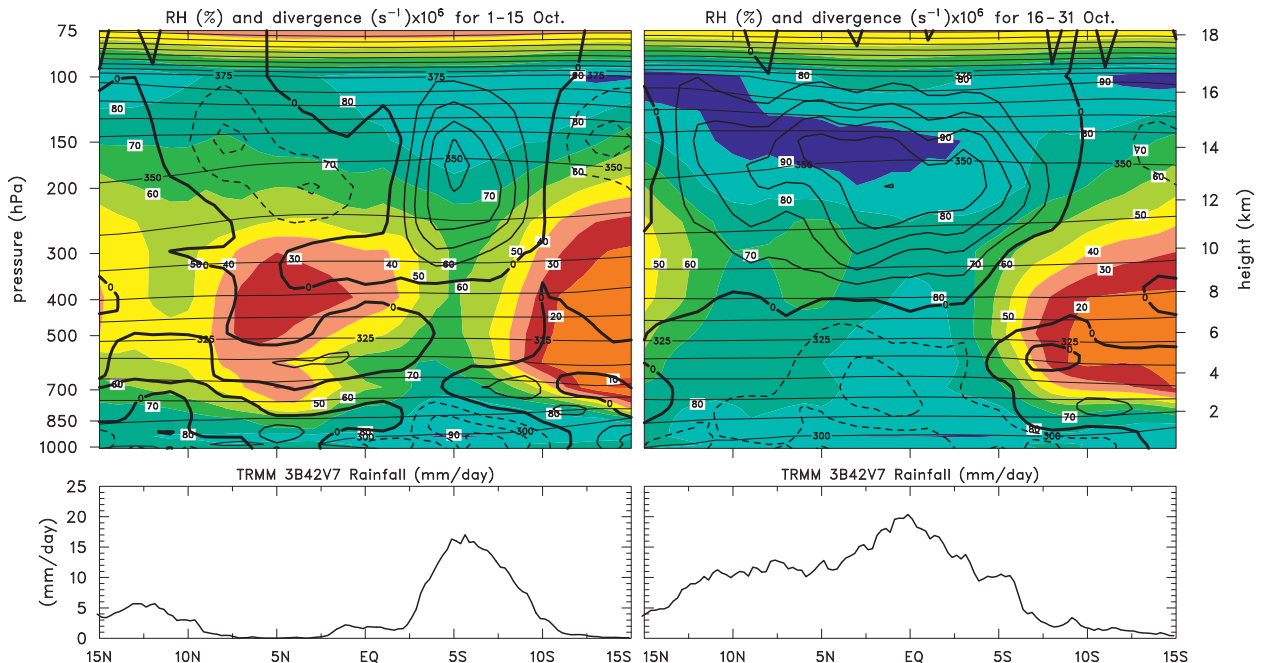


FIG. 21. North-south cross section through sounding arrays of ECMWF operational analysis (top) relative humidity (%; shading; with respect to ice for  $T < 0^\circ\text{C}$ ), horizontal divergence (contour interval =  $2 \times 10^{-6} \text{ s}^{-1}$ ), and potential temperature (K; thin quasi-horizontal lines; contour interval = 5 K); and (bottom) TRMM 3B42 rainfall for periods (left) 1-15 Oct and (right) 16-31 Oct 2011.

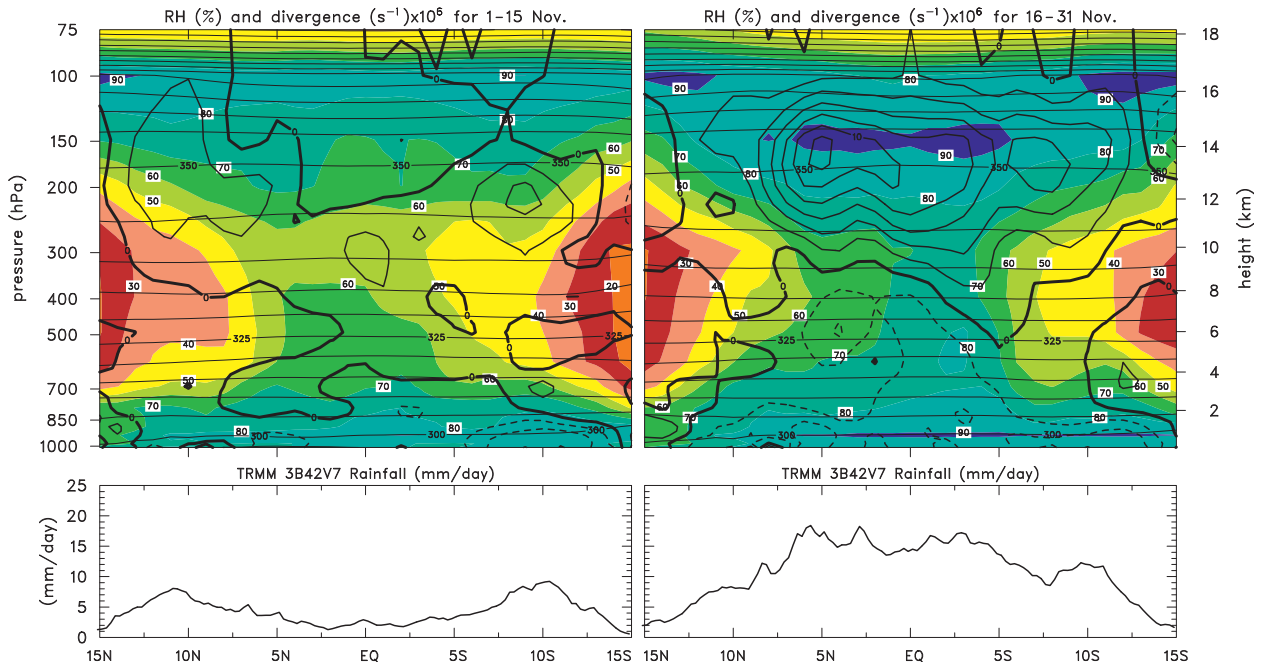


FIG. 22. As in Fig. 21, but for periods (left) 1–15 Nov and (right) 16–30 Nov 2011.

unrealistic features that were not representative of the individual events themselves.

This study has only explored the gross features of the October and November MJOs observed during

DYNAMO. Many details have yet to be investigated, particularly the processes leading to moistening of the lower troposphere prior to deep convection. That effort will require an integration of the results from the sounding

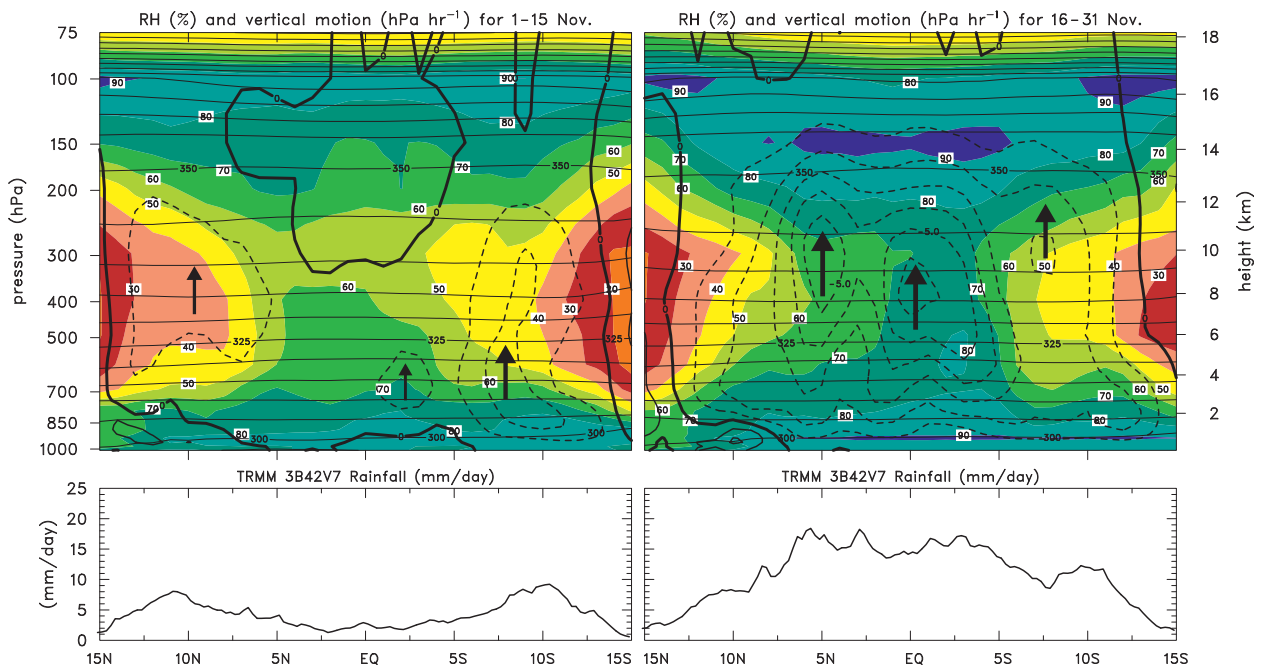


FIG. 23. North–south cross section through sounding arrays of ECMWF operational analysis (top) relative humidity (%; shading; with respect to ice for  $T < 0^{\circ}\text{C}$ ), vertical motion (contour interval =  $1\text{ hPa h}^{-1}$ ), and potential temperature (K, thin quasi-horizontal lines); and (bottom) TRMM 3B42 rainfall for periods (left) 1–15 Nov and (right) 16–30 Nov 2011.

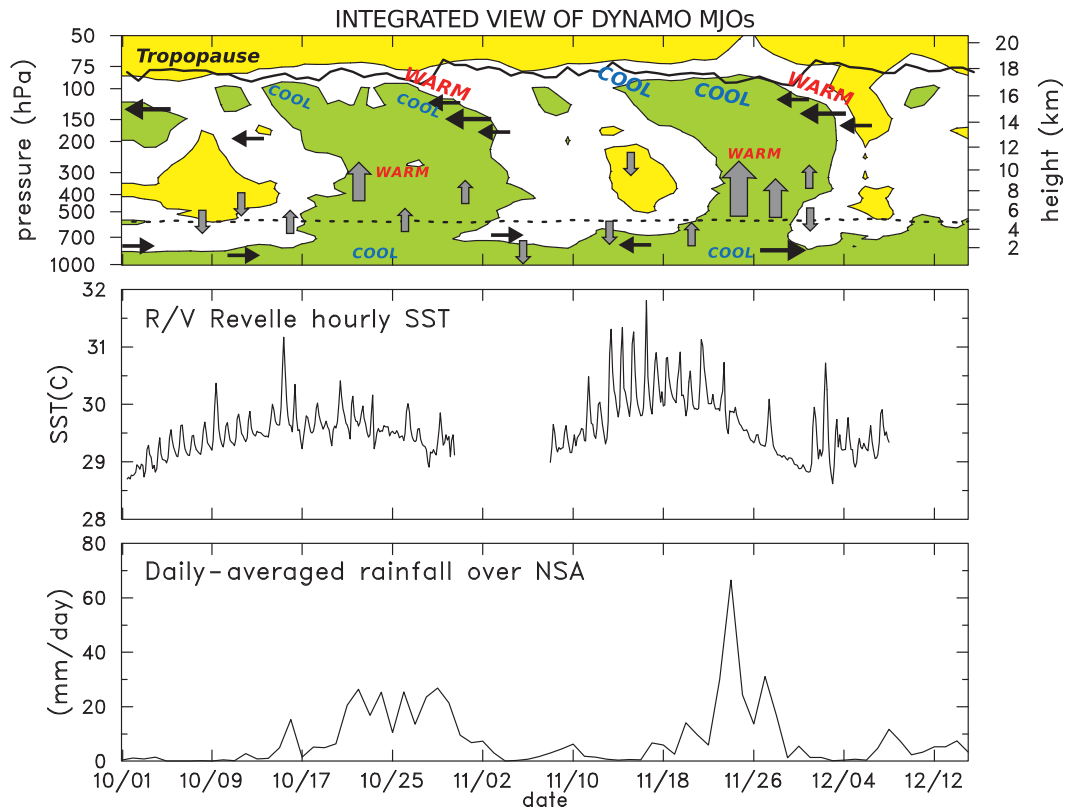


FIG. 24. (top) Integrated depiction of vertical structure of two MJOs during the period 1 Oct–15 Dec 2011 based on mean fields over the northern sounding array. Green (yellow) shading denotes areas of relative humidity greater than 70% (less than 40%), respectively. Thin (thick) arrows denote locations of zonal wind (vertical motion) maxima. Centers of cool and warm temperature anomalies are shown. Relative magnitudes of features are represented by sizes of symbols. At upper levels, these anomalies have a tilted structure as do the easterly wind maxima. Daily averaged  $0^{\circ}\text{C}$  level (dashed line) and cold-point tropopause level (solid line) are indicated. (middle) Hourly SST time series at R/V *Revelle*. (bottom) TRMM 3B42 daily averaged rainfall rate over the northern sounding array.

array with other DYNAMO/CINDY/AMIE observations, especially the evolving cloud and precipitation fields as determined by radars and lidars.

*Acknowledgments.* The success of the DYNAMO/CINDY/AMIE sounding campaign is a result of the substantial contributions and dedication of many individuals, including students and other staff from the United States, Taiwan, and Japan who helped with the operations at the various sounding sites. We thank Eric DeWeaver and Brad Smull of the National Science Foundation for supporting the sounding installation at Malé. We also thank Bill Brown, Masaki Katsumata, Scot Loehrer, Chuck Long, Jim Moore, June Wang, Steve Williams, Kunio Yoneyama, and Kate Young for assistance with both the field-phase and post-field phase sounding data support and processing. SST data from the *Revelle* were provided by James Edson, Chris Fairall, and Simon de Szoeke. The help of Rick Taft and Kathy Straub with figures is greatly appreciated. We thank

Chidong Zhang for valuable interactions throughout the campaign and Paul Roundy and two anonymous reviewers for helpful reviews of the manuscript. This research has been supported by the National Science Foundation under Grants AGS-1059899 and AGS-1138353.

#### REFERENCES

- Benedict, J., and D. A. Randall, 2007: Observed characteristics of the MJO relative to maximum rainfall. *J. Atmos. Sci.*, **64**, 2332–2354.
- , and —, 2009: Structure of the Madden–Julian oscillation in the superparameterized CAM. *J. Atmos. Sci.*, **66**, 3277–3296.
- Bladé, I., and D. L. Hartmann, 1993: Tropical intraseasonal oscillation in a simple nonlinear model. *J. Atmos. Sci.*, **50**, 2922–2939.
- Chen, S. S., R. A. Houze Jr., and B. E. Mapes, 1996: Multiscale variability of deep convection in relation to large-scale circulation in TOGA COARE. *J. Atmos. Sci.*, **53**, 1380–1409.
- Ciesielski, P. E., L. Hartten, and R. H. Johnson, 1997: Impacts of merging profiler and rawinsonde winds on TOGA COARE analyses. *J. Atmos. Oceanic Technol.*, **14**, 1264–1279.

- , R. H. Johnson, P. T. Haertel, and J. Wang, 2003: Corrected TOGA COARE sounding humidity data: Impact on diagnosed properties of convection and climate over the warm pool. *J. Climate*, **16**, 2370–2384.
- , and Coauthors, 2010: Quality controlled upper-air sounding dataset for TiMREX/SoWMEX: Development and corrections. *J. Atmos. Oceanic Technol.*, **27**, 1802–1821.
- Cronin, M. F., and M. J. McPhaden, 1997: The upper ocean heat balance in the western equatorial Pacific warm pool during September–December 1992. *J. Geophys. Res.*, **102**, 8533–8553.
- Del Genio, A. D., Y. Chen, D. Kim, and M.-S. Yao, 2012: The MJO transition from shallow to deep convection in *CloudSat/CALIPSO* and GISS GCM simulations. *J. Climate*, **25**, 3755–3770.
- Flatau, M., P. J. Flatau, P. Phoebus, and P. P. Niiler, 1997: The feedback between equatorial convection and local radiative and evaporative processes: The implication for intraseasonal oscillations. *J. Atmos. Sci.*, **54**, 2373–2386.
- Gill, A. E., 1980: Some simple solutions for heat-induced tropical circulation. *Quart. J. Roy. Meteor. Soc.*, **106**, 447–462.
- Godfrey, J. S., R. A. Houze Jr., R. H. Johnson, R. Lukas, J.-L. Redelsperger, A. Sui, and R. Weller, 1998: Coupled Ocean-Atmosphere Response Experiment: An interim report. *J. Geophys. Res.*, **103** (C7), 14 395–14 450.
- Hack, J. J., W. H. Schubert, D. E. Stevens, and H.-C. Kuo, 1989: Response of the Hadley Circulation to convective forcing in the ITCZ. *J. Atmos. Sci.*, **46**, 2957–2973.
- Haertel, P. T., and R. H. Johnson, 1998: Two-day disturbances in the equatorial western Pacific. *Quart. J. Roy. Meteor. Soc.*, **124**, 615–636.
- , G. N. Kiladis, A. Denno, and T. M. Rickenbach, 2008: Vertical-mode decompositions of 2-day waves and the Madden–Julian oscillation. *J. Atmos. Sci.*, **65**, 813–833.
- Hermes, J. C., and C. J. C. Reason, 2008: Annual cycle of the South Indian Ocean (Seychelles-Chagos) thermocline ridge in a regional ocean model. *J. Geophys. Res.*, **113**, C04035, doi:10.1029/2007JC004363.
- Hohenegger, C., and B. Stevens, 2013: Preconditioning deep convection with cumulus congestus. *J. Atmos. Sci.*, **70**, 448–464.
- Houze, R. A., Jr., 1982: Cloud clusters and large-scale vertical motion in the tropics. *J. Meteor. Soc. Japan*, **60**, 396–410.
- , 1989: Observed structure of mesoscale convective systems and implications for large-scale heating. *Quart. J. Roy. Meteor. Soc.*, **115**, 425–461.
- Hu, Q., and D. A. Randall, 1994: Low-frequency oscillations in radiative-convective systems. *J. Atmos. Sci.*, **51**, 1089–1099.
- Huffman, G. J., R. F. Adler, D. T. Bolvin, G. Gu, E. J. Nelkin, K. P. Bowman, E. F. Stocker, and D. B. Wolff, 2007: The TRMM Multisatellite Precipitation Analysis (TMPA): Quasi-global, multiyear, combined-sensor precipitation estimates at fine scales. *J. Hydrometeorol.*, **8**, 33–55.
- Hung, M.-P., J.-L. Lin, W. Wang, D. Kim, T. Shinoda, and S. J. Weaver, 2013: MJO and convectively coupled equatorial waves simulated by CMIP5 climate models. *J. Climate*, **26**, 6185–6214.
- Johnson, R. H., 1984: Partitioning tropical heat and moisture budgets into cumulus and mesoscale components: Implications for cumulus parameterization. *Mon. Wea. Rev.*, **112**, 1590–1601.
- , and X. Lin, 1997: Episodic trade wind regimes over the western Pacific warm pool. *J. Atmos. Sci.*, **54**, 2020–2034.
- , and P. E. Ciesielski, 2002: Characteristics of the 1998 summer monsoon onset over the northern South China Sea. *J. Meteor. Soc. Japan*, **80**, 561–578.
- , T. M. Rickenbach, S. A. Rutledge, P. E. Ciesielski, and W. H. Schubert, 1999: Trimodal characteristics of tropical convection. *J. Climate*, **12**, 2397–2418.
- Kalnay, E., and Coauthors, 1996: The NCEP/NCAR 40-Year Reanalysis Project. *Bull. Amer. Meteor. Soc.*, **77**, 437–471.
- Katsumata, M., P. E. Ciesielski, and R. H. Johnson, 2011: Evaluation of budget analysis during MISMO. *J. Appl. Meteor. Climatol.*, **50**, 241–254.
- Kemball-Cook, S. R., and B. C. Weare, 2001: The onset of convection in the Madden–Julian oscillation. *J. Climate*, **14**, 780–793.
- Kikuchi, K., and Y. N. Takayabu, 2004: The development of organized convection associated with the MJO during TOGA COARE IOP: Trimodal characteristics. *Geophys. Res. Lett.*, **31**, L10101, doi:10.1029/2004GL019601.
- Kiladis, G. N., K. H. Straub, G. C. Reid, and K. S. Gage, 2001: Aspects of interannual and intraseasonal variability of the tropopause and lower stratosphere. *Quart. J. Roy. Meteor. Soc.*, **127**, 1961–1984.
- , —, and P. T. Haertel, 2005: Zonal and vertical structure of the Madden–Julian oscillation. *J. Atmos. Sci.*, **62**, 2790–2809.
- Kim, H.-M., C. D. Hoyos, P. J. Webster, and I. S. Kang, 2009: Ocean–atmosphere coupling and the boreal winter MJO. *Climate Dyn.*, **35**, 771–784, doi:10.1007/s00382-009-0612-x.
- Lau, W. K.-M., and D. E. Waliser, 2005: *Intraseasonal Variability of the Atmosphere–Ocean Climate System*. Springer, 474 pp.
- Liebmann, B., and C. A. Smith, 1996: Description of a complete (interpolated) outgoing longwave radiation dataset. *Bull. Amer. Meteor. Soc.*, **77**, 1275–1277.
- Lin, J.-L., B. E. Mapes, M. Zhang, and N. Newman, 2004: Strati-form precipitation, vertical heating profiles, and the Madden–Julian oscillation. *J. Atmos. Sci.*, **61**, 296–309.
- , and Coauthors, 2006: Tropical intraseasonal variability in 14 IPCC AR4 climate models. Part I: Convective signals. *J. Climate*, **19**, 2665–2690.
- Lin, X., and R. H. Johnson, 1996: Kinematic and thermodynamic characteristics of the flow over the western Pacific warm pool during TOGA COARE. *J. Atmos. Sci.*, **53**, 695–715.
- Lukas, R., and E. Lindstrom, 1991: The mixed layer of the western equatorial Pacific Ocean. *J. Geophys. Res.*, **96**, 3343–3357.
- Madden, R. A., and P. R. Julian, 1972: Description of global-scale circulation cells in the tropics with a 40–50 day period. *J. Atmos. Sci.*, **29**, 1109–1123.
- Maloney, E. D., 2009: The moist static energy budget of a composite tropical intraseasonal oscillation in a climate model. *J. Climate*, **22**, 711–729.
- , and D. L. Hartmann, 1998: Frictional moisture convergence in a composite life cycle of the Madden–Julian oscillation. *J. Climate*, **11**, 2387–2403.
- Mapes, B. E., and R. A. Houze Jr., 1995: Diabatic divergence profiles in western Pacific mesoscale convective systems. *J. Atmos. Sci.*, **52**, 1807–1828.
- , S. Tulich, J. Lin, and P. Zuidema, 2006: The mesoscale convection life cycle: Building block or prototype for large-scale tropical waves? *Dyn. Atmos. Oceans*, **42**, 3–29.
- Matthews, A. J., 2008: Primary and successive events in the Madden–Julian Oscillation. *Quart. J. Roy. Meteor. Soc.*, **134**, 439–453.
- Meyers, G., P. McIntosh, L. Pigot, and M. Pook, 2007: The years of El Niño, La Niña, and interactions with the tropical Indian Ocean. *J. Climate*, **20**, 2872–2880.
- Mori, S., and Coauthors, 2004: Diurnal land–sea rainfall peak migration over Sumatera Island, Indonesian Maritime Continent,

- observed by TRMM satellite and intensive rawinsonde soundings. *Mon. Wea. Rev.*, **132**, 2021–2039.
- Nakazawa, T., 1988: Tropical super clusters within intraseasonal variations over the western Pacific. *J. Meteor. Soc. Japan*, **66**, 823–839.
- Reynolds, R. W., T. M. Smith, C. Liu, D. B. Chelton, K. S. Casey, and M. G. Schlax, 2007: Daily high-resolution-blended analyses for sea surface temperature. *J. Climate*, **20**, 5473–5496.
- Riley, E. M., B. E. Mapes, and S. N. Tulich, 2011: Clouds associated with the Madden–Julian oscillation: A new perspective from *CloudSat*. *J. Atmos. Sci.*, **68**, 3032–3051.
- Roundy, P. E., 2012a: Observed structure of convectively coupled waves as a function of equivalent depth: Kelvin waves and the Madden–Julian oscillation. *J. Atmos. Sci.*, **69**, 2097–2106.
- , 2012b: The spectrum of convectively coupled Kelvin waves and the Madden–Julian oscillation in regions of low-level easterly and westerly background flow. *J. Atmos. Sci.*, **69**, 2107–2111.
- , and L. M. Gribble-Verhagen, 2010: Variations in the flow of the global atmosphere associated with a composite convectively coupled oceanic Kelvin wave. *J. Climate*, **23**, 4192–4201.
- , C. J. Schreck III, and M. A. Janiga, 2009: Contributions of convectively coupled equatorial Rossby waves and Kelvin waves to the real-time multivariate MJO indices. *Mon. Wea. Rev.*, **137**, 469–478.
- Sakurai, N., and Coauthors, 2005: Diurnal cycle of cloud system migration over Sumatera Island. *J. Meteor. Soc. Japan*, **83**, 835–850.
- Schubert, W. H., P. E. Ciesielski, D. E. Stevens, and H.-C. Kuo, 1991: Potential vorticity modeling of the ITCZ and the Hadley Circulation. *J. Atmos. Sci.*, **48**, 1493–1509.
- Schumacher, C., R. A. Houze Jr., and I. Kraucunas, 2004: The tropical dynamical response to latent heating estimates derived from the TRMM precipitation radar. *J. Atmos. Sci.*, **61**, 1341–1358.
- Shinoda, T., and H. H. Hendon, 1998: Mixed layer modeling of intraseasonal variability in the tropical western Pacific and Indian Oceans. *J. Climate*, **11**, 2668–2685.
- Small, R. J., and Coauthors, 2008: Air–sea interaction over ocean fronts and eddies. *Dyn. Atmos. Oceans*, **45**, 274–319.
- Stephens, G. L., P. J. Webster, R. H. Johnson, R. Engelen, and T. S. L’Ecuyer, 2004: Observational evidence for the mutual regulation of the tropical hydrological cycle and the tropical sea surface temperatures. *J. Climate*, **17**, 2213–2224.
- Straub, K. H., 2013: MJO initiation in the real-time multivariate MJO index. *J. Climate*, **26**, 1130–1151.
- , and G. N. Kiladis, 2002: Observations of a convectively coupled Kelvin wave in the eastern Pacific ITCZ. *J. Atmos. Sci.*, **59**, 30–53.
- Takayabu, Y. N., K.-M. Lau, and C.-H. Sui, 1996: Observation of a quasi-2-day wave during TOGA COARE. *Mon. Wea. Rev.*, **124**, 1892–1913.
- Tam, C.-Y., and N.-C. Lau, 2005: Modulation of the Madden-Julian Oscillation by ENSO: Inference from observations and GCM simulations. *J. Meteor. Soc. Japan*, **83**, 727–743.
- Vialard, J., and Coauthors, 2009: CIRENE: Air–sea interactions in the Seychelles–Chagos thermocline ridge region. *Bull. Amer. Meteor. Soc.*, **90**, 45–61.
- Virts, K. S., and J. M. Wallace, 2010: Annual, interannual, and intraseasonal variability of tropical tropopause transition layer cirrus. *J. Atmos. Sci.*, **67**, 3113–3129.
- , —, Q. Fu, and T. P. Ackerman, 2010: Tropical tropopause transition layer cirrus as represented by *CALIPSO* lidar observations. *J. Atmos. Sci.*, **67**, 3113–3129.
- Waite, M. L., and B. Khouider, 2010: The deepening of tropical convection by congestus preconditioning. *J. Atmos. Sci.*, **67**, 2601–2615.
- Waliser, D. E., 2006: Intraseasonal variability. *The Asian Monsoon*, B. Wang, Ed., Springer, 203–257.
- Wang, B., 2005: Theory. *Intraseasonal Variability in the Atmosphere–Ocean Climate System*, W. K. M. Lau and D. E. Waliser, Eds., Springer, 19–61.
- Wang, J., and L. Zhang, 2008: Systematic errors in global radiosonde precipitable water data from comparisons with ground-based GPS measurements. *J. Climate*, **21**, 2218–2238.
- , H. L. Cole, D. J. Carlson, E. R. Miller, K. Beierle, A. Paukkunen, and T. K. Laine, 2002: Corrections of the humidity measurement errors from the Vaisala RS80 radiosonde—Application to TOGA COARE data. *J. Atmos. Oceanic Technol.*, **19**, 981–1002.
- , L. Zhang, A. Dai, F. Immler, and H. Vömel, 2013: Radiation dry bias correction of Vaisala RS92 humidity data and its impact on historical radiosonde data. *J. Atmos. Oceanic Technol.*, **30**, 197–214.
- Webster, P. J., C. A. Clayson, and J. A. Curry, 1996: Clouds, radiation, and the diurnal cycle of sea surface temperature in the tropical western Pacific. *J. Climate*, **9**, 1712–1730.
- , A. Moore, J. Loschnigg, and M. Leban, 1999: Coupled ocean–atmosphere dynamics in the Indian Ocean during 1997–98. *Nature*, **401**, 356–360.
- Weller, R. A., and S. P. Anderson, 1996: Surface meteorology and air–sea fluxes in the western equatorial Pacific warm pool during the TOGA Coupled Ocean–Atmosphere Response Experiment. *J. Climate*, **9**, 1959–1990.
- Wheeler, M. C., and K. M. Weickmann, 2001: Real-time monitoring and prediction of modes of coherent synoptic to intraseasonal tropical variability. *Mon. Wea. Rev.*, **129**, 2677–2694.
- , and H. H. Hendon, 2004: An all-season real-time multivariate MJO index: Development of an index for monitoring and prediction. *Mon. Wea. Rev.*, **132**, 1917–1932.
- Xie, S.-P., 2004: Satellite observations of cool ocean–atmosphere interaction. *Bull. Amer. Meteor. Soc.*, **85**, 195–208.
- Yamada, H., K. Yoneyama, M. Katsumata, and R. Shirooka, 2010: Observations of a super cloud cluster accompanied by synoptic-scale eastward-propagating precipitating systems over the Indian Ocean. *J. Atmos. Sci.*, **67**, 1456–1473.
- Yoneyama, K., and Coauthors, 2008: MISMO field experiment in the equatorial Indian Ocean. *Bull. Amer. Meteor. Soc.*, **89**, 1889–1903.
- , C. Zhang, and C. N. Long, 2013: Tracking pulses of the Madden–Julian oscillation. *Bull. Amer. Meteor. Soc.*, in press.
- Yu, L., and R. A. Weller, 2007: Objectively analyzed air–sea heat fluxes for the global oceans (1981–2005). *Bull. Amer. Meteor. Soc.*, **88**, 527–539.
- Yuan, J., and R. A. Houze Jr., 2013: Deep convective systems observed by A-Train in the tropical Indo-Pacific region affected by the MJO. *J. Atmos. Sci.*, **70**, 465–486.
- Zhang, C., 2005: Madden-Julian Oscillation. *Rev. Geophys.*, **43**, RG2003, doi:10.1029/2004RG000158.
- , J. Gottschalck, E. D. Maloney, M. W. Moncrieff, F. Vitart, D. E. Waliser, B. Wang, and M. C. Wheeler, 2013: Cracking the MJO nut. *Geophys. Res. Lett.*, **40**, 1223–1230, doi:10.1002/grl.50244.